

A Simulation Study of the Lithium Ion Transport Mechanism in Ternary Polymer Electrolytes – The Critical Role of the Segmental Mobility

Diddo Diddens^{1,2,*} and Andreas Heuer^{1,2}

¹*Institut für physikalische Chemie, Westfälische Wilhelms-Universität
Münster, Corrensstrasse 28/30, 48149 Münster, Germany*

²*NRW Graduate School of Chemistry, Corrensstrasse 36, 48149 Münster, Germany*
(Dated: June 30, 2021)

We present an extensive molecular dynamics (MD) simulation study of the lithium ion transport in ternary polymer electrolytes consisting of poly(ethylene oxide) (PEO), lithium-bis(trifluoromethane)sulfonimide (LiTFSI) and the ionic liquid *N*-methyl-*N*-propylpyrrolidinium bis(trifluoromethane)sulfonimide (PYR₁₃TFSI). In particular, we focus on two different strategies by which the ternary electrolytes can be devised, namely by (a) *adding* the ionic liquid to PEO₂₀LiTFSI, and (b) *substituting* the PEO chains in PEO₂₀LiTFSI by the ionic liquid. In order to grasp the changes of the overall lithium transport mechanism, we employ an analytical, Rouse-based cation transport model (Maitra *et al.*, *Phys. Rev. Lett.*, **2007**, 98, 227802), which has originally been devised for binary PEO-based electrolytes. This model distinguishes three different microscopic transport mechanisms, each quantified by an individual time scale. In the course of our analysis, we extend this mathematical description to account for an entirely new transport mechanism, namely the TFSI-supported diffusion of lithium ions decoupled from the PEO chains, which emerges for certain stoichiometries. We find that the segmental mobility plays a decisive role in PEO-based polymer electrolytes. That is, whereas the addition of the ionic liquid to PEO₂₀LiTFSI plasticizes the polymer network and thus also increases the lithium diffusion, the amount of free, mobile ether oxygens reduces when substituting the PEO chains by the ionic liquid, which compensates the plasticizing effect. In total, our observations allow us to formulate some general principles about the lithium ion transport mechanism in ternary polymer electrolytes. Moreover, our insights also shed light on recent experimental observations (Joost *et al.*, *Electrochim. Acta*, **2012**, 86, 330).

PACS numbers:

I. INTRODUCTION

Polymer electrolytes – typically consisting of an amorphous polymer matrix and a salt dissolved in it¹ – are promising candidates for many technological devices such as batteries or fuel cells²⁻⁴. Here, a commonly used polymer is poly(ethylene oxide) (PEO), whereas lithium-bis(trifluoromethane)sulfonimide (LiTFSI) is often employed as conducting salt, as the large TFSI anion reduces ion aggregation. However, at ambient temperatures, the conductivity is still too low for an efficient technological use.

Several attempts have been made in the past to overcome this deficiency. Common modifications of the classical polymer-salt systems are the addition of nanoparticles⁵ or organic solvent molecules⁶⁻⁸. However, in case of the latter, the resulting electrolytes suffer from the high volatility and thus flammability of the solvent as well as from its reaction with lithium metal electrodes⁸. Here, Passerini *et al.*⁹⁻¹² demonstrated that the use of an ionic liquid (IL) instead of a conventional solvent has several advantages: The ILs are non-volatile, non-flammable¹³ and exhibit a wide electrochemical stability window¹⁴⁻¹⁶. In this way, improved polymer electrolytes can be designed, which show an increased conductivity combined with inherent stability^{9,12}, and are thus ideal to create light-weighted but powerful batteries^{10,11}.

In a recent molecular dynamics (MD) simulation

study¹⁷, we investigated a ternary polymer electrolyte consisting of PEO₂₀LiTFSI and a variable mole fraction x of the IL *N*-methyl-*N*-propylpyrrolidinium bis(trifluoromethane)sulfonimide (PYR₁₃TFSI). As observed experimentally by Passerini *et al.*^{9,12}, we also found a clear increase of the lithium diffusion coefficient with x , and were able to show that the main reason for this enhancement can be attributed to the plasticization of the PEO backbone by the IL. That is, the presence of the IL enhances the PEO dynamics, and consequently, the lithium ions coordinated to the PEO backbone also become faster.

In this contribution, we will significantly expand the scope of our previous analysis¹⁷, and investigate the lithium transport in ternary polymer electrolytes in a more general way. This is not only due to the fact that we present additional insights on the ternary PEO₂₀LiTFSI· x PYR₁₃TFSI mixtures (in which IL is *added* to binary PEO₂₀LiTFSI), but also follow a conceptually different approach how to create ternary polymer electrolytes, that is, we also *substitute* PEO chains in PEO₂₀LiTFSI by PYR₁₃TFSI molecules. This procedure is carried out in such a way that the overall lithium volume concentration is held constant. Figure 1 shows snapshots from the simulations for the two different scenarios. The motivation for our extended study is twofold: First, although Passerini *et al.* found in their recent work¹² that the lithium diffusion coefficient increases with the IL fraction for an ether oxygen-to-lithium ion (EO : Li) ratio

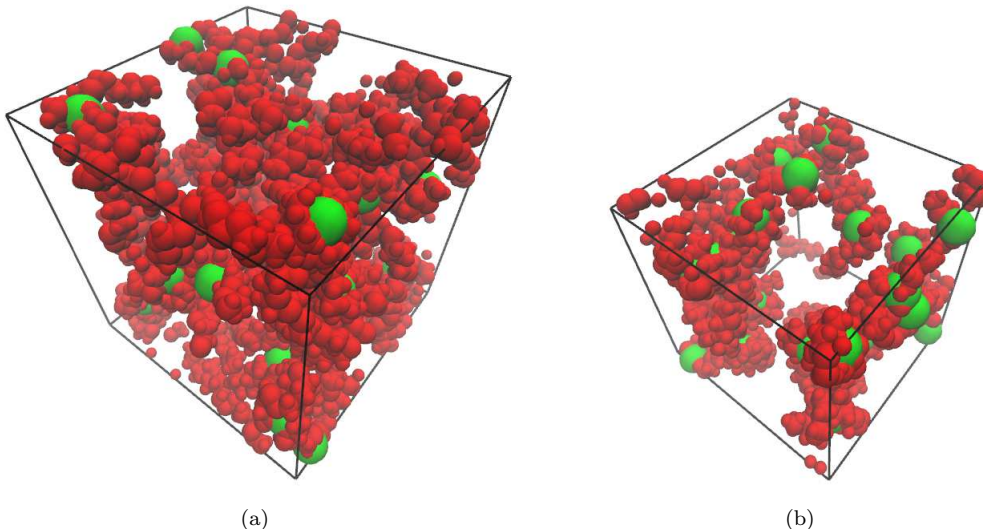


Figure 1: Snapshots from the simulation showing (a) the *addition* of IL to the binary polymer electrolyte $\text{PEO}_{20}\text{LiTFSI}$ and (b) the *substitution* of PEO chains by IL molecules from the same electrolyte. PEO chains are shown in red, lithium ions in green, whereas all other ions (PYR_{13}^{+} and TFSI^{-}) are invisible.

of 20 : 1, they simultaneously observed no significant changes for lower ratios of 10 : 1 or 5 : 1. This observation becomes even more puzzling by additional insights from Raman measurements¹², which revealed that with increasing x , the lithium-TFSI coordination increases at the expense of the lithium-PEO coordination (especially for low EO : Li ratios). Although these findings rather suggest a lithium transport mechanism which is at least partly decoupled from the PEO chains, it is obvious from the approximately constant lithium diffusion coefficients that the lithium motion cannot be similar to that in pure IL/LiTFSI electrolytes, which would be significantly faster^{18,19}. Nevertheless, the transport mechanism has to change at some point when PEO is successively replaced by $\text{PYR}_{13}\text{TFSI}$ molecules, which gives us a second, theoretical motivation for our extended study. Thus, the concentration series of the PEO substitution serves as a model electrolyte in a double sense, as both the EO : Li ratio decreases with increasing IL fraction, while at the same time a crossover from a PEO-based lithium transport mechanism to a TFSI-based transport mechanism is enforced.

In addition to the MD simulations, we also employ an analytical ion transport model²⁰ to clarify the issues outlined above. This model expresses the macroscopic lithium diffusion in PEO-based polymer electrolytes via three different microscopic mechanisms, each characterized by a specific time scale (see sketch in Figure 2): 1. Diffusion along the PEO chain, which can be interpreted as an effective one-dimensional random walk along the curvilinear path of the polymer chain. This motion can be characterized by the time scale τ_1 the ion needs to explore the entire PEO chain. 2. Segmental motion of the PEO chain, which can be separated into the center-of-mass motion and the internal dynamics. For non-

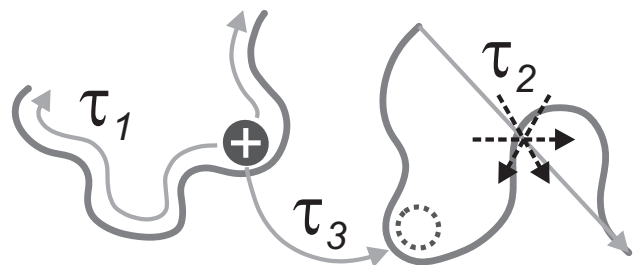


Figure 2: Sketch depicting the three different cation transport mechanisms in PEO-salt electrolytes. Each mechanism is characterized by a specific time scale.

entangled chains, the internal dynamics can be described by the Rouse model²¹ via an effective Rouse time τ_2 , characterizing the motion of the bound PEO segments. 3. Intersegmental transfer of the cation from one PEO chain to another, which can be quantified by the average residence time τ_3 at a given chain. Previous simulations²⁰ have shown that this mechanism can be viewed as a renewal process within the framework of the Dynamic Bond Percolation (DBP) model²², since the dynamics of a given lithium ion becomes independent of its past after being transferred to another PEO chain. One particular advantage of our model is that it allows one to extrapolate the lithium diffusion coefficients derived from the numerical data to the experimentally relevant long-chain limit.

However, one should keep in mind that the ion transport model has originally been developed for the archetypal, binary polymer electrolytes. Although our previous study¹⁷ showed that the lithium transport mechanism qualitatively remains the same for the case of IL addi-

tion, it is a priori unclear if this also holds for the PEO substitution, as the transport mechanism will certainly change at some point when PEO is removed from the electrolyte. In fact, it will turn out that the IL-mediated lithium transport may substantially contribute to the overall lithium migration, and we will propose a revised model accounting for this additional, fourth transport mechanism.

Further advancements compared to our original study¹⁷ are comprehensive analyses related to the microscopic factors contributing to the individual transport mechanisms. For example, we will demonstrate that the plasticization by the IL is only one important requirement to yield an enhanced segmental mobility and thus a faster lithium diffusion. Moreover, the effect of the IL on the polymer dynamics is also interesting from a fundamental point of view, as it gives rise to hydrodynamic interactions among distinct PEO segments, reflected by a Zimm-like scaling of the Rouse-mode relaxation times. Concerning the other mechanisms, we will show that e. g. the renewal process (characterized by τ_3) can be understood in terms of a few structural and dynamical observables. These additional insights could ultimately contribute to a more directed improvement of battery materials.

For all ternary electrolytes, PEO₂₀LiTFSI will be used as a reference. In what follows, the electrolytes with a constant EO : Li ratio, i. e. 20 : 1, and a variable amount x of PYR₁₃TFSI will be denoted as PEO₂₀LiTFSI · x PYR₁₃TFSI. The new electrolyte types, devised to study the differences in the lithium transport mechanisms between binary PEO/LiTFSI and PYR₁₃TFSI/LiTFSI, will be denoted as PEO_{20- α x}LiTFSI · x PYR₁₃TFSI. Here, α is the ratio of the respective partial molar volumes of a PYR₁₃TFSI ion pair and a PEO monomer (see below).

For reasons of simplicity, we also abbreviate PEO as ‘P’ (i. e. polymer or PEO) and LiTFSI as ‘S’ (i. e. salt) in the following, leading to the short-hand notations P₂₀S · x IL and P_{20- α x}S · x IL for the two distinct classes of ternary electrolytes.

This article is organized as follows: Section II describes the details of the MD simulation procedure and the setup of the systems. In Section III, we discuss the lithium ion coordination sphere and the structure of the PEO chains. Section IV deals with the two transport processes involving changes in the lithium coordination sphere (intersegmental transfer and diffusion along the chain), followed by a detailed analysis of the polymer dynamics (Section V). Having characterized all three transport mechanisms, we compare the predictions of our model with the experimental data from Passerini *et al.*¹² (Section VI). Finally, we conclude (Section VII).

II. MD SIMULATION METHODOLOGY

The MD simulations were performed with a modified version of the sander module of the AMBER package²³, allowing us to use a force field specifically designed for PEO/LiTFSI^{24,25} and PYR₁₃TFSI²⁶ (see appendix, Section B for a validation of the modified AMBER code and Section C for a benchmark assessing its performance).

The initial configurations were created by randomly placing the individual molecules on a simple cubic lattice with a lattice constant of 36 Å irrespective of their type, mixing the system in this way. In case of PEO, the chains already had coiled conformations as under melt conditions, thereby circumventing an expensive equilibration.

The binary PEO/LiTFSI electrolyte contained 10 PEO chains with $N = 54$ monomers each as well as 27 LiTFSI molecules. In case of the addition of IL, i. e. P₂₀S · x IL, the simulation cell also contained 18 ($x = 0.66$) or 87 ($x = 3.24$) PYR₁₃TFSI molecules. The latter system is shown in Figure 1(a). In case of the substitution of PEO (P_{20- α x}S · x IL) and thus a constant lithium volume concentration, the partial molar volumes of PEO and PYR₁₃TFSI must be known. Through several short equilibration runs of the respective binary electrolytes, namely PEO _{n} LiTFSI ($n = 30, 20$ and 10) and PYR₁₃TFSI · x LiTFSI ($x = 0.20, 0.24$ and 0.26) in the NpT ensemble, we found that the molar volumes of both PEO and PYR₁₃TFSI are independent of the LiTFSI fraction for the investigated concentration ranges. Their ratio reveals that approximately $\alpha = 7.14$ PEO monomers occupy the same volume as one PYR₁₃TFSI ion pair. Based on this value, we created the following systems: 8 PEO chains with 15 PYR₁₃TFSI molecules (P₁₆S · 0.556 IL), 6 PEO chains with 30 PYR₁₃TFSI molecules (P₁₂S · 1.111 IL), and 4 PEO chains with 45 PYR₁₃TFSI molecules (P₈S · 1.667 IL, see Figure 1(b)), all of them containing, as above, 27 LiTFSI ion pairs. Neat PEO (16 chains with $N = 54$) and the pure PYR₁₃TFSI/LiTFSI electrolyte (76 PYR₁₃TFSI molecules and 27 LiTFSI ion pairs, PYR₁₃TFSI · 0.262 LiTFSI) serve as reference within this context.

The systems were equilibrated in the NpT ensemble for 70 – 80 ns using the PME technique²⁷. Afterwards, production runs with a total length of 200 ns were performed in the NVT ensemble. A time step of 1 fs was used in all simulations to propagate the systems. The temperature was maintained by the Berendsen thermostat²⁸ with a reference temperature of 423 K. All bonds involving hydrogen were constrained by the SHAKE algorithm²⁹. The inducible point dipoles were integrated by a Car-Parrinello-like scheme³⁰, and the charge-dipole interactions between atoms separated by three bonds (1-4 interactions) were scaled by a factor of 0.2. For all other nonbonded contributions, the full 1-4 interaction was taken into account. Dipole-dipole interactions were damped using a Thole screening³¹ with a dimensionless damping parameter²⁴ of $a_T = 0.4$.

system	r_1	r_2	b_0^2 [Å ²]	$\langle \mathbf{R}_e^2 \rangle$ [Å ²]	$\langle \mathbf{R}_g^2 \rangle$ [Å ²]
PEO	-	-	10.4	1904 ± 43	306 ± 35
P ₂₀ S	0.47	0.53	9.7	1573 ± 112	260 ± 42
P ₂₀ S · x IL					
P ₂₀ S · 0.66 IL	0.53	0.47	9.7	1654 ± 121	272 ± 38
P ₂₀ S · 3.24 IL	0.76	0.24	9.6	1498 ± 57	249 ± 37
P _{20-αx} S · x IL					
P ₁₆ S · 0.556 IL	0.55	0.45	9.5	1767 ± 271	267 ± 50
P ₁₂ S · 1.111 IL	0.64	0.35	9.3	1349 ± 150	227 ± 43
P ₈ S · 1.667 IL	0.84	0.14	9.1	1840 ± 430	280 ± 80

Table I: Fraction of lithium ions coordinating to one (r_1) or two (r_2) PEO chains, mean squared chemical bond length b_0^2 , mean squared end-to-end vector $\langle \mathbf{R}_e^2 \rangle$ and mean squared radius of gyration $\langle \mathbf{R}_g^2 \rangle$ of the PEO chains.

Table VI (appendix) shows the average values of the box lengths as determined from the NpT runs and subsequently used in the NVT simulations. One indeed observes that box length is nearly the same for all P_{20- α x}S · x IL systems. Slight deviations for PYR₁₃TFSI · 0.262 LiTFSI may result from rounded molecule numbers in the simulation.

III. STRUCTURAL PROPERTIES

A. Lithium Coordination

In order to quantify the local structure around the lithium ions, radial distribution functions (denoted as $g(r)$ in the following) have been computed for the atom pairs Li⁺-O_{PEO} and Li⁺-O_{TFSI} (see A 2). Both coordination types exhibit a sharp peak around 2 Å, corresponding to the first coordination shell, which is in good agreement with neutron diffraction experiments³² and quantum chemistry calculations^{33,34}. At larger distances no significant structural arrangement can be found. When successively adding the IL, one observes that the peak positions of both Li⁺-O_{PEO} and Li⁺-O_{TFSI} remain the same for all electrolytes. Thus, the same criterion to define temporary lithium bonds will be used for the subsequent analysis. We consider a EO and a Li⁺ as bound if their distance is not larger than 3.0 Å. In analogy, we consider a Li⁺ and a TFSI oxygen as bound if their distance is not larger than 2.7 Å.

The probability distribution functions to find a lithium ion with a certain number of EOs or TFSI oxygens in its first coordination shell is also shown in the appendix (Figure 11). To summarize, we find that the predominant lithium coordination consists of 4 – 5 EOs for all electrolytes, which is again in good agreement with the experimental data³² and the quantum-chemical results^{33,34}. In those complexes where the 4 – 5 EOs originate from a single PEO molecule, the polymer chain wraps helically around the cation. For complexes involving two PEO chains, typically 2 – 3 EOs from each chain coordinate to the ion.

Coordinations by TFSI oxygens are mostly rare, and often the anion coordinates only briefly to the lithium ion (cf. Figure 1, where all ions are in the vicinity of a PEO chain). The only exceptions are P₈S · 1.667 IL and, though less pronounced, P₁₂S · 1.111 IL. Here, the lithium ions more likely coordinate to 1 – 2 TFSI oxygens in contrast to all other systems, and some are even coordinated to TFSI only (0.4 % for P₁₂S · 1.111 IL and 2.5 % for P₈S · 1.667 IL). As in pure IL/LiTFSI, the prevalent coordination number in the latter scenario is about 3 – 4 TFSI oxygens, originating mostly from different anions. This specific coordination has also been observed previously in MD simulations³⁵, although experimental work emphasizes that also the Li(TFSI)₂ complex is important³⁶.

Table I summarizes the fraction of lithium ions coordinating to one or two PEO chains (denoted as r_1 and r_2 , respectively). Coordinations to three PEO chains were rarely observed and had a very brief life time of a few picoseconds only. Therefore, these events were neglected for the subsequent analysis. For the pure polymer electrolyte, the fractions of complexes involving one and two chains are nearly equal. Similar binding energies for both coordination types have also been found in quantum chemistry calculations³⁴. The fraction of lithium ions coordinating to one PEO molecule increases with the IL content for both types of electrolytes.

In case of P₂₀S · x IL, this is a consequence of the reduced PEO concentration, as it becomes less likely that a lithium ion encounters a second chain in the semidilute case. This is also confirmed by the observation that the fraction of Li⁺ coordinating to one PEO chain increases linearly with x , showing that the changes in the coordination sphere are purely statistical.

For P_{20- α x}S · x IL, however, these trends are stronger than linear, which can be attributed to the fact that the PEO chains are successively removed from the system, and the remaining PEO chains become more crowded by Li⁺ (see below). Thus, the different coordination shell can not solely be explained as a simple dilution effect.

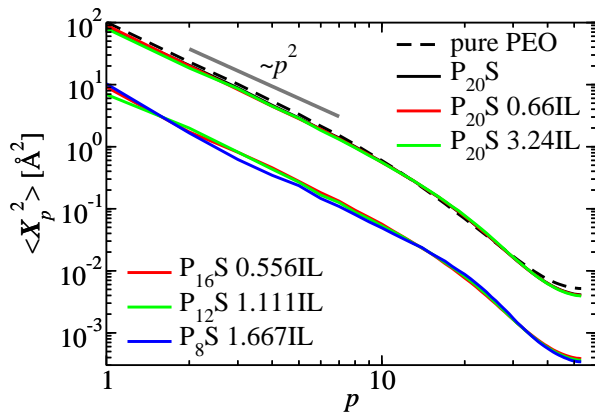


Figure 3: Rouse mode amplitudes $\langle \mathbf{X}_p^2 \rangle$ in dependence of the mode number p calculated from the expression of the discrete Rouse model, i. e. $\mathbf{X}_p(t) = (1/N) \sum_{n=1}^N \cos((p\pi(n - 1/2)/N)) \mathbf{R}_n(t)$. The curves of the $P_{20-\alpha x}S \cdot x$ IL electrolytes have been shifted by one order of magnitude.

B. Statical Polymer Structure

Due to the helical coordination structure of the PEO backbone, the local polymer structure changes, and the conformational phase space of the chain is reduced. Moreover, in case of the ternary electrolytes, the additional IL molecules dilute the PEO chains, thus inducing a crossover from a polymer melt to a semidilute solution, which may also alter the equilibrium conformation of the polymer chains³⁷. Table I summarizes the mean squared distance b_0^2 between two chemical monomers and the mean squared end-to-end vector $\langle \mathbf{R}_e^2 \rangle$. Due to the crown-ether-like coordination of the PEO backbone, b_0^2 is smaller in all lithium-containing systems. For $P_{20-\alpha x}S \cdot x$ IL, this trend becomes more pronounced with increasing IL concentration.

A contraction of the polymer chain can also be observed for $P_{20}S \cdot x$ IL from $\langle \mathbf{R}_e^2 \rangle$, which also decreases, whereas for $P_{20-\alpha x}S \cdot x$ IL no clear predictions can be made within the statistical uncertainties. When determining the ratio of $\langle \mathbf{R}_e^2 \rangle$ and the radius of gyration $\langle \mathbf{R}_g^2 \rangle$ (Table I), one finds values close to the ideal ratio of six for a Gaussian chain³⁷ for all electrolytes, again indicating that on a global scale the chains are approximately Gaussian.

Also for the scaling of the Rouse mode amplitudes $\langle \mathbf{X}_p^2 \rangle$, we observe only slight deviations from the respective curve for pure PEO (Figure 3). Here, the modes \mathbf{X}_p were determined from the simulation data using the respective expression of the discrete Rouse model³⁸, i. e. $\mathbf{X}_p(t) = (1/N) \sum_{n=1}^N \cos(p\pi(n - 1/2)/N) \mathbf{R}_n(t)$, where the \mathbf{R}_n denote the position vectors of the individual monomers. In the limit of low mode numbers p , we find the expected Rousean scaling $\langle \mathbf{X}_p^2 \rangle \propto p^{-2}$, again demonstrating that the chain structure remains relatively ideal upon the addition of IL. Thus, no significant swelling of the chains can be observed, and the structural properties

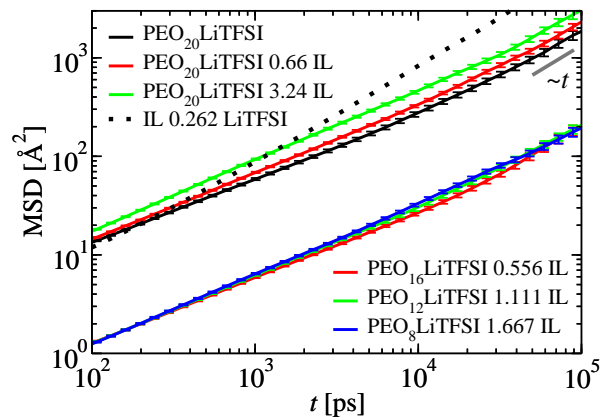


Figure 4: MSDs of the lithium ions in the individual electrolytes. The curves of the $P_{20-\alpha x}S \cdot x$ IL electrolytes have been shifted by one order of magnitude. The curve for the pure IL-salt solution $\text{PYR}_{13}\text{TFSI} \cdot 0.262 \text{LiTFSI}$ is also shown for comparison.

are similar as in neat PEO. On a local scale however, the PEO chains become rather contracted due to the helical coordination sphere of the lithium ions.

IV. LITHIUM DYNAMICS

The MSDs of the lithium ions in the individual electrolytes are shown in Figure 4. For $P_{20}S \cdot x$ IL, one indeed observes an increase of the lithium mobility upon the addition of IL. In particular, this increase becomes visible at 1 – 10 ns, whereas the onset to diffusive behavior occurs on the same time scale for all systems. Nevertheless, the MSDs are much smaller than for pure $\text{PYR}_{13}\text{TFSI} \cdot 0.262 \text{LiTFSI}$, and the crossover to diffusion occurs much later. This is consistent with the observation that nearly all cations coordinate to the PEO chains, and that the lithium transport in the ternary electrolytes changes not too drastically as compared to $P_{20}S$. Interestingly, for $P_{20-\alpha x}S \cdot x$ IL, no significant difference in the lithium MSD can be found.

In the following, we will employ the lithium ion transport model in order to rationalize these observations. First, we will focus on the intersegmental transfer and the diffusion along the chain, followed by an in-detail analysis of the polymer dynamics. Once all ingredients are combined, we will use the transport model to compute the macroscopic lithium diffusion coefficients from the numerical data, and compare these values to the experimental data from Passerini *et al.*¹².

A. Lithium Ion Transfer Mechanism

First, we will study the lithium ion transfer between two different polymer chains, which is vital for the long-range cation transport and thus any macroscopically

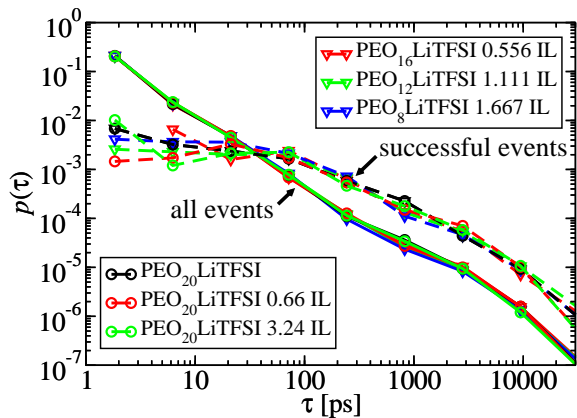


Figure 5: Histogram of the life times τ of the intermediate complexes involving two PEO chains which facilitate the cationic transfer. Solid: all events, dashed: successful events only (see text).

measurable lithium diffusion. That is, when only considering the diffusion along the chain and the PEO dynamics as possible transport mechanisms, the ion remains confined to a finite volume characterized by the radius of gyration of the PEO chains. Moreover, the diffusion of the center of mass of the polymer chain becomes irrelevant in the experimentally relevant long-chain limit. Previous MD simulations focusing on this mechanism have shown that the dynamics of the lithium ion is independent from its past after such a transfer processes²⁰, leading to Markovian behavior for time scales larger than τ_3 , and that these processes can thus be regarded as renewal events in the spirit of the DBP model²².

We start with the investigation of the detailed mechanism of the cation transfer process. During most transfers, the ion is coordinated to two PEO chains simultaneously (i. e. the leaving chain and the entering chain) as a transition state. In some events, the cation is also temporarily coordinated by TFSI anions only and migrates to another PEO chain in this way, which will be discussed below.

Figure 5 shows a histogram of the life times τ of the intermediate in which a Li^+ is coordinated by two PEO chains (solid lines). One clearly observes that the resulting distribution is very broad. Whereas most complexes exist only briefly (i. e. a few picoseconds), some exist over nearly the whole simulation length of 200 ns. For all electrolytes, no significant difference can be found for $p(\tau)$, suggesting a rather universal mechanism. This is also reasonable when keeping in mind that the lithium coordination sphere containing two PEO chains is relatively compact, and that the surrounding molecules thus hardly affect the transfer process once the complex has formed.

Of course, it is questionable if also the brief coordinations in Figure 5 can result in a successful cation transfer, since the separation of the leaving chain and the simultaneous formation of a new, stable coordination sphere

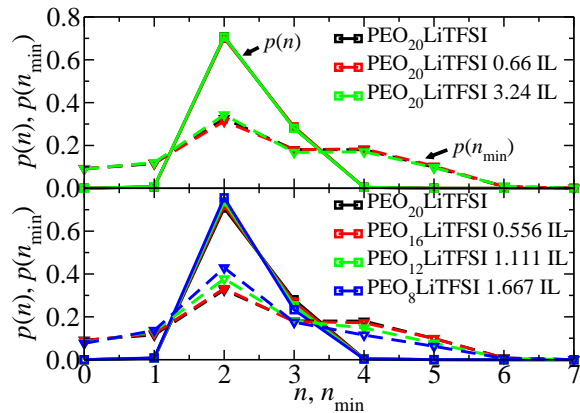


Figure 6: Probability $p(n)$ to find a specific EO coordination number n for a cation coordinated to two PEO chains (solid) as well as the probability $p(n_{\min})$ to find a minimum EO coordination number n_{\min} on the first PEO chain during the life time of the complex (dashed).

on the entering chain will need a certain time. For this purpose, Figure 5 also shows $p(\tau)$ for complexes which resulted in a successful transfer. The criterion for a successful transfer was that the lithium ion remained detached from the old chain for at least 100 ps, which was motivated by a more detailed analysis revealing that non-Markovian, short-time backjumps to the old chain occur up to about 100 ps (not shown). From Figure 5 one indeed observes that the probability for short τ is lower for real renewal events (dashed lines). Again, the curves are nearly identical for all electrolytes.

In order to study the transfer mechanism in more detail, we monitored the progress of the cation transfer as follows: When a second PEO chain enters the coordination sphere of a cation that is already coordinated to a PEO molecule, the EO coordination number n at the first chain naturally decreases. For brief coordinations of the second chain, the crown-ether-like structure of the first chain will hardly be perturbed. On the other hand, for longer times, one would expect a rather symmetric coordination by both PEO chains, leading to smaller n . In case of a successful cation transfer, the EO coordination number decreases even further to zero. The minimum coordination number n_{\min} that is reached during τ can therefore be used to monitor the progress and the success of the cation transfer.

Figure 6 shows the probability $p(n_{\min})$ to find a specific minimum coordination number n_{\min} as well as the probability to find any coordination number n on the first PEO chain during τ . One clearly observes that on average 2 – 3 EOs of each chain coordinate to the Li^+ (solid lines). This coordination is independent from the IL concentration as expected from the dense packing of the coordination sphere. For $p(n_{\min})$, one notices that the brief coordinations corresponding to $n_{\min} = 4 - 5$ become less likely with increasing IL concentration for $\text{P}_{20-\alpha x}\text{S} \cdot x \text{ IL}$. As a consequence, the relative probabil-

ity that a complex with $n_{\min} = 2$ is formed increases. For $P_{20}S \cdot x$ IL, no such effect can be observed, and $p(n_{\min})$ remains basically unaltered by the presence of the IL. This indicates that the increased probability of $n_{\min} = 2$ for $P_{20-\alpha x}S \cdot x$ IL is not related to a simple concentration effect, which would also be present for $P_{20}S \cdot x$ IL, but rather to the fact that the PEO molecules are successively substituted by IL. Due to this substitution, each PEO chain coordinates to more cations, resulting in an enhanced rigidity of the PEO backbone, which impedes the formation of the helical structure with $n = 4 - 5$ and thus leads to a larger value for $p(n_{\min} = 2)$.

In total, a complete cation transfer with $n_{\min} = 0$ has the same relative probability of about 10 % for all IL concentrations and EO : Li ratios. Obviously, the critical step is the encounter of a second PEO chain, or, more precisely, a free PEO segment. Once the complex has formed, it decays according to a universal distribution of life times (Figure 5). A remarkable feature, however, is the fact that although $p(n_{\min} = 2)$ (which corresponds to a symmetric coordination by both PEO chains) for $P_{20-\alpha x}S \cdot x$ IL increases with x , the complete transfer with $p(n_{\min} = 0)$ does not become more likely, indicating that other, less trivial factors affect the outcome of a PEO-Li⁺-PEO encounter.

It is also worth noting that, in contrast to earlier findings from MD simulations of a PEO/LiBF₄ electrolyte²⁰, no significant influence of the anion on the PEO-to-PEO transfer could be observed. Most likely, the minor importance of the TFSI anions for the transfer arises from the suppressed tendency to form ion pairs or higher-order ionic clusters as compared to BF₄⁻.

B. Renewal Time

In order to determine τ_3 , we counted the number of transfer processes N_{trans} from the simulations. As above, brief transfers and successive backjumps after less than 100 ps were excluded, while on the other hand transfer processes via the anions were also counted, since they serve as a renewal process in the same way. Subsequently, the τ_3 -values were determined according to $\tau_3 = t_{\max} N_{\text{Li}^+} / N_{\text{trans}}$, where $t_{\max} = 200$ ns is the simulation length and $N_{\text{Li}^+} = 27$ is the number of lithium ions in the simulation box.

The individual values for τ_3 are summarized in Table II. One observes for both the $P_{20}S \cdot x$ IL and the $P_{20-\alpha x}S \cdot x$ IL electrolytes that τ_3 increases with increasing IL concentration. Since the PEO molecules become more and more diluted, this can at least partly be explained as a concentration effect. However, the stronger increase for $P_{20-\alpha x}S \cdot x$ IL indicates that not only the reduced PEO concentration, but also the reduced number of free EOs, which are necessary for a successful transfer, leads to an increase of τ_3 . To understand these trends in more detail, we will figure out the individual contributions to the τ_3 -values in the following. When the

lithium ion moves through the electrolyte, it has to encounter a free PEO segment in order to be transferred (naturally, above the glass-transition temperature, the segments themselves also show significant motion). The probability for such an event can be estimated on the basis a few structural parameters: First, the volume element into which the Li⁺ moves has to be occupied by PEO. Here, the probability to encounter any PEO segment (free or bound) can be obtained from the volume fraction of PEO in the simulation cell, i. e. V_{PEO}/V . Second, the PEO segment has to be free, which is necessary to form the helical coordination sphere. Here, we defined a free segment as a block of at least four free EOs, which occurs with probability $p_{\text{PEO}}^{\text{free}}$. The overall probability to encounter a free PEO segment (at least four EOs) is then given by the product of V_{PEO}/V and $p_{\text{PEO}}^{\text{free}}$ (both quantities are shown in Table II). Apart from these structural ingredients, one also needs dynamical information how fast the PEO segments (and the attached lithium ions) move. That is, the faster both the lithium ions and the PEO segments rearrange, the more opportunities the ions have to find a free PEO segment and to be transferred. Although the effect of the IL on the polymer dynamics will be discussed in Section V, we nevertheless use the parameter C_R (Table III), which is the prefactor of the Rouse-like MSD $\propto t^{1/2}$ for the average EOs, as an anticipatory measure for the polymer dynamics. Since C_R quantifies the motion of the average EOs, it implicitly contains the dynamics of both the free PEO segments and the lithium ions (due to the cooperative motion with the bound EOs, which are also contained in C_R ; see below). When plotting the product $(V_{\text{PEO}}/V) p_{\text{PEO}}^{\text{free}} C_R$ versus the observed τ_3 , we find a nearly perfect linear relationship (correlation coefficient -0.99) within the statistical error of τ_3 . This demonstrates that τ_3 is essentially determined by three factors: the volume fraction of PEO and the fraction of free PEO segments (or, alternatively, the volume concentration of free PEO segments) on one hand, and the polymer dynamics on the other hand.

Table II also shows the probability $p_{\text{trans,IL}}$ that a TFSI-supported transfer takes place ($p_{\text{trans,IL}} = N_{\text{trans,IL}}/N_{\text{trans}}$; i. e. the number of transfers in which the Li⁺ is intermediately coordinated to TFSI only relative to the total number of transfers). For high IL concentrations, it becomes more likely for a lithium ion to migrate through the IL-rich regions of the electrolyte. Since this scenario is less likely for $P_{20}S \cdot x$ IL, one can conclude that the transfer via TFSI in $P_{20-\alpha x}S \cdot x$ IL is mainly caused by the crowded PEO chains and the lower fraction of free EOs. Also shown in Table II is the mean time $\langle \tau_{\text{Li}} \rangle_{\text{IL}}$ the Li⁺ is coordinated to TFSI only in a PEO-TFSI-PEO transfer, and the average squared distance $\langle \Delta \mathbf{R}_{\text{Li}}^2 \rangle_{\text{IL}}$ the lithium ion covers during this period. The values for $\langle \tau_{\text{Li}} \rangle_{\text{IL}}$ and $\langle \Delta \mathbf{R}_{\text{Li}}^2 \rangle_{\text{IL}}$ show similar trends as $p_{\text{trans,IL}}$: With increasing IL fraction and decreasing number of free EOs ($P_{20-\alpha x}S \cdot x$ IL electrolytes), both $\langle \tau_{\text{Li}} \rangle_{\text{IL}}$ and $\langle \Delta \mathbf{R}_{\text{Li}}^2 \rangle_{\text{IL}}$ show a significant increase. From the Einstein relation $D_{\text{Li,IL}} = \langle \Delta \mathbf{R}_{\text{Li}}^2 \rangle_{\text{IL}} / (6 \langle \tau_{\text{Li}} \rangle_{\text{IL}})$, we

system	τ_3 [ns]	V_{PEO}/V	$p_{\text{EO}}^{\text{free}}$ [%]	p_{IL} [%]	$p_{\text{trans,IL}}$ [%]	$\langle\tau_{\text{Li}}\rangle_{\text{IL}}$ [ns]	$\langle\Delta\mathbf{R}_{\text{Li}}^2\rangle_{\text{IL}}$ [\AA^2]
P ₂₀ S	17.1 ± 1.3	0.87	72.3	0.02	2.5	0.25 ± 0.08	31 ± 8
P ₂₀ S · x IL							
P ₂₀ S · 0.66 IL	18.4 ± 1.4	0.72	71.9	0.03	1.0	0.58 ± 0.31	34 ± 13
P ₂₀ S · 3.24 IL	24.1 ± 1.3	0.43	73.1	0.36	8.5	0.99 ± 0.22	102 ± 26
P _{20-αx} S · x IL							
P ₁₆ S · 0.556 IL	25.0 ± 2.0	0.70	65.2	0.07	4.6	0.38 ± 0.14	34 ± 10
P ₁₂ S · 1.111 IL	28.4 ± 2.2	0.52	54.7	0.43	13.7	0.88 ± 0.20	79 ± 17
P ₈ S · 1.667 IL	32.7 ± 2.5	0.35	36.7	2.50	38.2	2.10 ± 0.31	226 ± 51

Table II: Average residence times τ_3 of a lithium ion at a given PEO chain. Here, $p_{\text{trans,IL}}$ is the probability that the lithium ion is transferred by TFSI anions, $\langle\tau_{\text{Li}}\rangle_{\text{IL}}$ corresponds to the average duration the Li^+ is coordinated to TFSI only in such a transfer, and $\langle\Delta\mathbf{R}_{\text{Li}}^2\rangle_{\text{IL}}$ is the average squared distance the ion covers during this time.

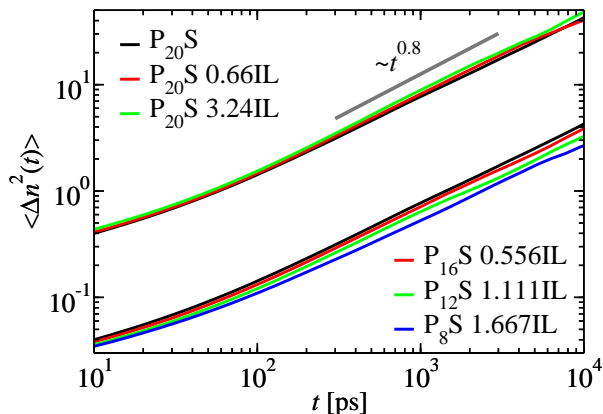


Figure 7: Mean square change of the average EO index $\langle\Delta n^2(t)\rangle$ for the P₂₀S · x IL and P_{20- α x}S · x IL electrolytes. The curves of the P_{20- α x}S · x IL electrolytes have been shifted by one order of magnitude.

find values close to the lithium diffusion coefficient in PYR₁₃TFSI · 0.262 LiTFSI ($D_{\text{Li,IL}} = 14.014 \text{ \AA}^2\text{ns}^{-1}$). Thus, for P_{20- α x}S · x IL, a change of the entire lithium transport mechanism becomes visible, and the PEO-TFSI-PEO transitions may substantially contribute to the overall lithium MSD for sufficiently large values of $p_{\text{trans,IL}}$ and $\langle\Delta\mathbf{R}_{\text{Li}}^2\rangle_{\text{IL}}$. On the other hand, from the probability p_{IL} to find a lithium ion coordinated to TFSI only at *any* time (Table II), one can conclude that the impact of the IL-mediated transport is negligible for most investigated electrolytes (see discussion in Section VI).

C. Diffusion along the Chain

In order to quantify the quasi-one-dimensional random walk of the lithium ions along the PEO chains, all EOs have been numbered consecutively, and the mean squared change $\langle\Delta n^2(t)\rangle$ of the average EO index n has been computed (Figure 7).

Starting from about 100 ps, the dynamics crosses over to a regime that is only slightly subdiffusive (i. e. $\langle\Delta n^2(t)\rangle \propto t^{0.8}$). Qualitatively, this behavior is found for

all compositions. For P₂₀S · x IL, no significant change of $\langle\Delta n^2(t)\rangle$ can be observed when varying the IL concentration, indicating that the motion along the chain is basically determined by the characteristic motion of the PEO backbone, and that the surrounding molecules (i. e. PEO chains or IL molecules) have virtually no influence on this mechanism. Interestingly, the magnitude of $\langle\Delta n^2(t)\rangle$ is essentially the same for lithium ions bound to one or to two PEO chains (not shown).

Switching to P_{20- α x}S · x IL, one observes that the motion along the chain becomes slower with increasing IL concentration, especially for P₁₂S · 1.111 IL and P₈S · 1.667 IL (Figure 7), which can be attributed to the lower fraction of free EOs in the system. Interestingly, the value for the exponent of $\langle\Delta n^2(t)\rangle$ remains basically the same in this case, and only the magnitude of the functional form $\langle\Delta n^2(t)\rangle \propto t^{0.8}$ becomes slightly lower.

In principle, this type of motion could be quantified by the respective diffusion coefficient D_1 extracted from Figure 7 according to the Einstein relation

$$D_1 = \lim_{t \rightarrow \infty} \frac{\langle\Delta n^2(t)\rangle}{2t}. \quad (1)$$

Unfortunately, the $\langle\Delta n^2(t)\rangle$ -curves in Figure 7 are not purely diffusive, whereas on larger time scales the statistics are too bad, since the ions are additionally transferred between distinct PEO chains, thus making it impossible to track the motion along the chain any further. In order to estimate the net effect of this mechanism, i. e. the number of traversed monomers during τ_3 , D_1 was approximately estimated as

$$D_1(\tau_3) = \frac{\langle\Delta n^2(\tau_3)\rangle}{2\tau_3}. \quad (2)$$

Since the maximum observation time in Figure 7 is lower than the τ_3 -values, we assumed that the scaling $\langle\Delta n^2(t)\rangle \propto t^{0.8}$ persists until $t = \tau_3$, and simply extrapolated the curves in Figure 7. Subsequently, the time scale τ_1 was calculated by the respective expression from the transport model²⁰:

$$\tau_1 = \frac{(N-1)^2}{\pi^2 D_1} \quad (3)$$

system	τ_1 [ns]	$\langle \mathbf{R}_e^2 \rangle_{\text{eff}}$ [\AA^2]	τ_R [ns]	τ_2 [ns]	C_R [$\text{\AA}^2 \text{ ns}^{-1/2}$]	C_2 [$\text{\AA}^2 \text{ ns}^{-1/2}$]
PEO	-	1979	22	-	151.5	-
P ₂₀ S	147	1662	45	167	89.0	46.2
P ₂₀ S · <i>x</i> IL						
P ₂₀ S · 0.66 IL	140	1570	37	89	92.7	59.8
P ₂₀ S · 3.24 IL	127	1571	24	68	115.2	68.4
P _{20-αx} S · <i>x</i> IL						
P ₁₆ S · 0.556 IL	181	1479	43	145	81.0	44.1
P ₁₂ S · 1.111 IL	208	1359	35	145	82.5	40.5
P ₈ S · 1.667 IL	301	1151	28	104	78.1	40.5

Table III: Parameters characterizing the two intramolecular transport mechanisms (see text for further explanation). The values for pure PEO are also shown for comparison.

Table III summarizes the resulting τ_1 -values. For the P_{20- αx} S · *x* IL electrolytes, one clearly observes an increase of τ_1 with increasing IL concentration, since more and more EOs become involved in complexes with lithium, and the PEO backbone becomes less mobile. Contrarily, for the P₂₀S · *x* IL electrolytes, τ_1 decreases only slightly, which can mainly be attributed to the dependence of τ_1 on τ_3 (Equation 2). In total, the motion along the chain basically remains unaltered in these electrolytes, as also suggested by Figure 7.

V. POLYMER DYNAMICS

A. Segmental Dynamics

In order to quantify the segmental polymer motion, the MSDs $\langle \Delta \mathbf{R}^2(t) \rangle$ of the EOs relative to the center of mass of the PEO chain have been calculated (Figure 8). This quantity has been computed for all EOs (i. e. irrespective of the presence of an ion), for EOs bound to a lithium ion and for the respective attached ions. The criterion to consider a cation or EO as bound was that the average EO index of the ion did not change more than one, i. e. $|\Delta n(t)| \leq 1$ for all time frames during t . For the bound EOs, no further distinction between additional coordinations of the lithium ion to e. g. another PEO chain or a TFSI molecule was made. Thus, these effects are already implicitly contained in the curves in Figure 8. Of course, one might wonder if cations bound to two PEO molecules show the same dynamical characteristics as ions bound to single polymer chain, as the Li(PEO)₂ complexes could be viewed as temporary crosslinks. A more detailed analysis (published in the appendix of our previous study¹⁷) indeed revealed that there is a conceptual difference between these two coordinations. However, the temporary crosslinks do not affect the polymer dynamics, but rather the motion along the chain: Whereas lithium ions coordinated to one chain are transported by both intramolecular mechanisms, ions bound to two chains experience the polymer dynamics only. This is due to the fact that the PEO chains move reptation-like along their own con-

tour past the cation, which results in a non-zero $\langle \Delta n^2(t) \rangle$ (Figure 7), but does not contribute to the overall lithium transport. Since there is no qualitative effect of the coordination on the polymer dynamics (possibly also due to the fact that the exchange between both coordination types is sufficiently fast), we proceed to characterize the average dynamics of the bound PEO segments with a single τ_2 only.

The average EOs (circles) show typical Rouse-like motion with the characteristic relaxation time τ_R . The dynamics of the bound EOs (diamonds) is qualitatively the same but protracted. Therefore, it is possible to characterize the intramolecular dynamics of the bound EOs by using a larger, effective Rouse time τ_2 . The lithium ions attached to these EOs (inset, solid lines) closely follow the bound EOs, which gives evidence for their cooperative motion. On short time scales, the MSD of the EOs is larger than the lithium MSD due to the additional internal degrees of freedom of the PEO backbone, but the MSD of the bound cations catches up on longer time scales (approximately 1 ns). Due to the collective motion, τ_2 also characterizes the dynamics of the attached lithium ions.

Figure 8 also shows the Rouse fits

$$\langle \Delta \mathbf{R}^2(t) \rangle = \frac{2 \langle \mathbf{R}_e^2 \rangle}{\pi^2} \sum_{p=1}^{\infty} \frac{[1 - \exp(-\frac{tp^2}{\tau_R})]}{p^2} \quad (4)$$

for the average (dashed lines) and the bound EOs (dotted lines). It is important to mention that the precise value of τ_2 obtained from these fits also depends on the value of $\langle \mathbf{R}_e^2 \rangle$ entering the prefactor of Equation 4. In order to obtain a fit consistent with the plateau value at large t , the MSDs of the average EOs were fitted using two parameters, i. e. τ_R and $\langle \mathbf{R}_e^2 \rangle_{\text{eff}}$. In this way, the $\langle \mathbf{R}_e^2 \rangle$ -values in Table I are replaced by an effective mean squared end-to-end vector $\langle \mathbf{R}_e^2 \rangle_{\text{eff}}$, characterizing the maximum accessible intramolecular distance for the cations. Once $\langle \mathbf{R}_e^2 \rangle_{\text{eff}}$ was determined from the MSDs of the average EOs, the MSDs of the bound EOs were fitted using this value in combination with a single fit parameter τ_2 only. The fitting parameters $\langle \mathbf{R}_e^2 \rangle_{\text{eff}}$, τ_R and τ_2

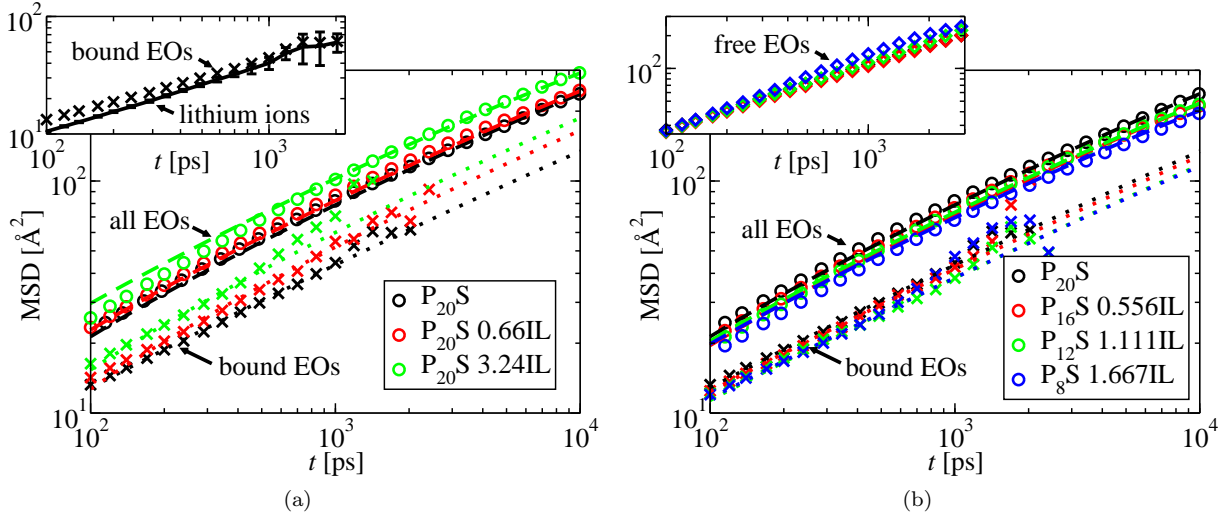


Figure 8: MSDs of the average EOs (circles), bound EOs (diamonds), lithium ions bound to these EOs ($|\Delta n(t)| \leq 1$, solid lines in the inset of Figure 8(a)). The inset of Figure 8(b) shows the MSD of the central EOs of a PEO segment consisting of at least seven free EOs. All MSDs have been computed in the center-of-mass frame of the PEO chain. The dashed and the dotted lines show the respective Rouse fits.

are summarized in Table III (deviations from our previous study³⁹ on $P_{20}S$ arise from the shorter simulation length of about 27 ns and the slightly modified fitting procedure).

In case of $P_{20}S \cdot x \text{ IL}$, $\langle \mathbf{R}_e^2 \rangle_{\text{eff}}$ decreases only slightly when IL is added. The $\langle \mathbf{R}_e^2 \rangle_{\text{eff}}$ -values are in reasonable agreement with the respective $\langle \mathbf{R}_e^2 \rangle$ -values in Table I. Compared to pure PEO, the $\langle \mathbf{R}_e^2 \rangle_{\text{eff}}$ are about 16 – 20 % lower in these systems and show good agreement with the respective values in Table I. This demonstrates that the PEO chains in these electrolytes behave relatively ideal, thus additionally validating our analysis in terms of the Rouse model. Both τ_R and τ_2 decrease significantly, clearly indicating that the dynamics of the PEO segments becomes faster with increasing IL concentration. Therefore, the IL can be regarded as plasticizer. Due to the enhanced polymer mobility, the lithium ions also move faster while they are coordinated to a specific chain, and the overall lithium MSD increases as observed in Figure 4. A similar observation has been made experimentally for other plasticizers like ethylene/propylene carbonate^{7,8} or short PEO chains embedded in a high-molecular weight matrix^{6,8}. Naturally, this effect has also been observed for ILs in the experiments¹² that motivated the present work.

For $P_{20-\alpha x}S \cdot x \text{ IL}$, $\langle \mathbf{R}_e^2 \rangle_{\text{eff}}$ clearly decreases when the PEO chains are successively substituted by IL molecules. The mismatch with the $\langle \mathbf{R}_e^2 \rangle$ -values in Table I results from the different averaging procedure: Whereas $\langle \mathbf{R}_e^2 \rangle$ is determined by the outer monomers only and thus rather characterizes the global polymer structure, $\langle \mathbf{R}_e^2 \rangle_{\text{eff}}$ contains contributions from all monomers, making it more susceptible to structural features on short and intermediate length scales. Note that the latter quantity is also statistically much better defined, since the average is taken

over all EOs instead of the outermost EOs only. The decrease of $\langle \mathbf{R}_e^2 \rangle_{\text{eff}}$ can be rationalized by the fact that more and more lithium ions coordinate to a specific PEO chain, thus diminishing the *average* intramolecular distances, and, consequently, the maximum accessible displacement for most ions. At the same time, it is still possible that the PEO chains are stretched on a global scale, which might arise from e.g. the electrostatic repulsion between distinct ions at a given chain (although for $P_{20-\alpha x}S \cdot x \text{ IL}$, one cannot make clear predictions within the uncertainties of $\langle \mathbf{R}_e^2 \rangle$ in Table I). In combination with the decline of $\langle \mathbf{R}_e^2 \rangle_{\text{eff}}$, the values for τ_R and τ_2 also decrease when the IL concentration is raised (Table III). However, it must be pointed out that the τ_R - and the τ_2 -values of different electrolytes can only be quantitatively compared in conjunction with the precise value of $\langle \mathbf{R}_e^2 \rangle_{\text{eff}}$. Therefore, a direct comparison of τ_R and τ_2 is only valid for similar $\langle \mathbf{R}_e^2 \rangle_{\text{eff}}$, as in the case of $P_{20}S \cdot x \text{ IL}$. This is also highlighted by the observations from Figure 8(b), where the EOs (both types) rather become slower with the IL fraction.

It is convenient to express $\langle \mathbf{R}_e^2 \rangle_{\text{eff}}$ and τ_R (or τ_2) within a single meaningful number. To this purpose, the prefactor of the characteristic Rouse-like motion for intermediate time scales (i.e. $\tau_R/N^2 \ll t \ll \tau_R$), $\langle \Delta \mathbf{R}^2(t) \rangle = (2\langle \mathbf{R}_e^2 \rangle / \pi^{3/2}) \sqrt{t/\tau_R}$, can be calculated, making it possible to directly measure the magnitude of the MSDs. Table III displays the constants $C_R = 2\langle \mathbf{R}_e^2 \rangle_{\text{eff}} / (\pi^3 \tau_R)^{1/2}$ and $C_2 = 2\langle \mathbf{R}_e^2 \rangle_{\text{eff}} / (\pi^3 \tau_2)^{1/2}$ for the individual systems, thereby quantifying the mobilities of the average and the bound EOs, respectively. Here, one indeed observes the same trends as from the direct comparison of the MSDs: For $P_{20}S \cdot x \text{ IL}$, the segmental mobility expressed by C_R and C_2 clearly increases with the IL concentration,

whereas it slightly decreases in case of the $P_{20-\alpha x}S \cdot x$ IL electrolytes, meaning that also the lithium dynamics decreases. This behavior can again be explained by the reduced flexibility of the PEO backbone, since the fraction of bound EOs increases when the PEO chains are gradually substituted by IL. Nevertheless, the plasticizing is also present for $P_{20-\alpha x}S \cdot x$ IL. This can be seen from the inset of Figure 8(b), which shows the MSDs of the central EOs of all those PEO segments consisting of at least seven free EOs. Again, one observes an increase in the polymer dynamics with increasing IL fraction. However, since the fraction of free EOs and the probability to encounter an entirely free PEO segment (cf. p_{EO}^{free} in Table II) is significantly lower, the plasticizing is barely visible in $P_{20-\alpha x}S \cdot x$ IL. Rather, for the average EOs, the progressive coordination of lithium ions to the PEO chains screens the plasticizing effect of the IL.

Finally, it is worth mentioning that for both investigated types of electrolytes, the center-of-mass dynamics of the PEO chains becomes faster with increasing IL concentration. (The impact of this increase on the lithium diffusion coefficient will be discussed in Section VI). However, this observation can be easily rationalized by the fact that motion of the individual chains is less hindered by other chains when the PEO concentration is reduced.

B. Hydrodynamic Interactions

An especially interesting effect of the IL on the polymer dynamics can be observed from the scaling of the Rouse mode relaxation times. The correlators $\langle \mathbf{X}_p(0)\mathbf{X}_p(t) \rangle$ display a stretched exponential relaxation (not shown), and a Kohlrausch-Williams-Watts fit, $\langle \mathbf{X}_p(0)\mathbf{X}_p(t) \rangle / \langle \mathbf{X}_p^2 \rangle = \exp(-(t/\hat{\tau}_p)^\beta)$, was used to extract the parameters $\hat{\tau}_p$ and β (here, the hats have been used to avoid confusion with the time scales τ_1 , τ_2 and τ_3 of the lithium ion transport model). The mean relaxation time $\langle \hat{\tau}_p \rangle$ is then given by $\langle \hat{\tau}_p \rangle = \hat{\tau}_p \beta^{-1} \Gamma(\beta^{-1})$, where Γ is the gamma function. The resulting scaling of $\langle \hat{\tau}_p \rangle$ is shown in Figure 9. Deviations from the values for $\tau_R \equiv \langle \hat{\tau}_1 \rangle$ in Table III result from the fact that the segmental MSD reflects an average over all modes, whereas $\langle \hat{\tau}_1 \rangle$ is determined from the first mode only.

For low mode numbers, both pure PEO as well as $P_{20}S$ exhibit the same scaling of approximately $\langle \hat{\tau}_p \rangle \propto p^{-2}$, thereby indicating that the global modes are Rousean. The absolute values of the $\langle \hat{\tau}_p \rangle$ are systematically higher for $P_{20}S$ due to the decelerating effect of the lithium ions.

In contrast to this, one observes a clear decrease of the relaxation times at low p for $P_{20}S \cdot 3.24$ IL as compared to $P_{20}S$. As already observed from the fits of the segmental MSDs (Figure 8), $P_{20}S \cdot 3.24$ IL approximately has the same value for τ_R as pure PEO, whereas the local $\langle \hat{\tau}_p \rangle$ ($p \gg 1$) are basically the same as for the binary $P_{20}S$. However, a faster global relaxation combined with a similar local relaxation can only be realized by a less steep dependence of $\langle \hat{\tau}_p \rangle$ on p . These observations are

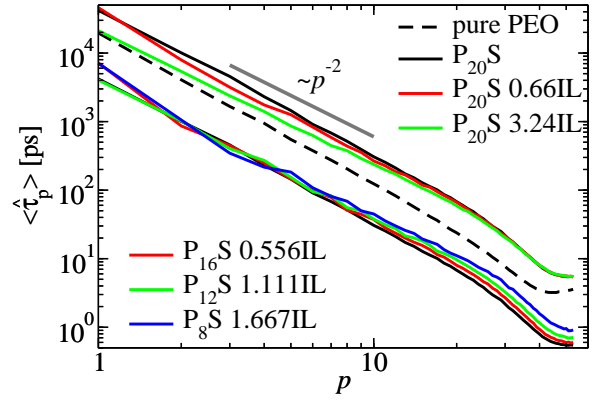


Figure 9: Average Rouse mode relaxation times $\langle \hat{\tau}_p \rangle$ in dependence of the mode number p . The curves of the $P_{20-\alpha x}S \cdot x$ IL electrolytes have been shifted by one order of magnitude.

compatible with a scenario in which hydrodynamic interactions, arising from the presence of the IL, contribute to the overall polymer motion. From an analytical point of view, these interactions can readily be taken into account via the Zimm model^{37,40}. In its simplest form, i. e. when no swelling of the chains is present (cf. $\langle \mathbf{R}_e^2 \rangle$ in Table I and $\langle \mathbf{X}_p^2 \rangle$ in Figure 3), the equilibrium distribution of the chain conformation is Gaussian as in the Rouse model. Therefore, the static polymer properties remain unaffected, and only the dynamics is altered, leading to a scaling of the relaxation times of $\hat{\tau}_p \propto p^{-3/2}$.

Interestingly, for $P_{20-\alpha x}S \cdot x$ IL, the scaling of the $\langle \hat{\tau}_p \rangle$ for intermediate p does not change significantly. However, the uncertainties of these curves increase when the PEO chains are successively replaced by IL (up to 60 % in the worst case, i. e. $p = 1$ for $P_8S \cdot 1.667$ IL). For the local modes, the $\langle \hat{\tau}_p \rangle$ increase with the IL concentration, again highlighting the reduced flexibility of the PEO backbone. Therefore, in total, the replacement of PEO by IL rather leads to a decrease of the polymer dynamics, and the plasticizing effect of the IL is not sufficient to compensate for the slowing down of the PEO segments caused by the attached lithium ions.

Although the scaling of the $\langle \hat{\tau}_p \rangle$ is rather Zimm-like⁴⁰ (i. e. $\langle \hat{\tau}_p \rangle \propto p^{-3/2}$) for $P_{20}S \cdot x$ IL, especially for $P_{20}S \cdot 3.24$ IL, the segmental MSD nevertheless shows the characteristic Rousean proportionality $MSD \propto t^{1/2}$ for $t \geq 1$ ns (Figure 8) instead of the respective Zimm scaling³⁷ $MSD \propto t^{2/3}$. Only on time scales up to about 1 ns, the MSD of the average EOs is lower and slightly steeper than the Rouse predictions for $P_{20}S \cdot 3.24$ IL. This is in clear contrast to $P_{20}S$, for which the PEO curve is larger than the Rouse prediction due to the additional internal degrees of freedom of the PEO backbone. Thus, this feature reflects another minor imprint of the hydrodynamic interactions. On larger length scales however, the hydrodynamic interactions are screened, since the monomer concentration in the PEO-IL solutions is still relatively high. Consequently, the chains interpenetrate strongly as

in the pure polymer melt, and the momentum transfer via the low-molecular solvent acts only on short length scales. A similar dynamical behavior has also been reported previously for semidilute solutions of model polymers⁴¹ simulated by a combination of stochastic Langevin dynamics and Lattice Boltzmann techniques⁴². Since the motion on larger scales is still Rousean, we also left Equation 4 unchanged in order to extract τ_2 for the P₂₀S · *x* IL electrolytes.

VI. COMPARISON WITH EXPERIMENTS

Finally, we compare the predictions of the lithium transport model to the experimental data taken from ref. 12. Of course, a direct comparison of D_{Li} as extracted from Figure 4 is impossible, since the center-of-mass motion of the short PEO chains ($N = 54$) in our simulations significantly contributes to the lithium diffusion, whereas most experimental studies focus on the long-chain limit (e. g. $M_w = 4,000,000$ g/mol in ref. 12). However, due the explicit N -dependence of the three time scales²⁰, i. e. $\tau_1 \propto N^2$, $\tau_2 \propto N^2$ and $\tau_3 \propto N^0$, and using the fact that the center-of-mass motion vanishes for $N \rightarrow \infty$, this problem can be easily circumvented.

For the scaling of τ_2 , entanglement effects may become relevant, which would manifest itself by a steeper dependence of the polymer relaxation time on N for chain lengths larger than the entanglement length N_e . However, if $\tau_3 < \tau_e$, meaning that the lithium ion leaves the chain before the latter begins to reptate, the dynamical contribution to the lithium ions is still Rousean³⁷. In the case of PEO, experiments revealed that the entanglement regime sets in from about $N \approx 75$ ^{43,44}. Based on these observations, one can estimate τ_e according to $\tau_e = \tau_R(N = 75) = \tau_R(75/54)^2$. For P₂₀S, this leads to $\tau_e \approx 87$ ns, which is substantially larger than τ_3 . Also in case of the highly plasticized P₂₀S · 3.24 IL one finds $\tau_e \approx 46$ ns $>$ τ_3 . Therefore, the lithium ion leaves the PEO chain before the tube constraints become noticeable, and the transport model can also be applied in the limit of long chains.

Due to the renewal events (i. e. the interchain transfer), D_{Li} can be expressed as

$$D_{\text{Li}}(N) = \frac{\langle g_{12}(N, \tau_3) \rangle_{\text{M3}}}{6\tau_3} + D_{\text{PEO}}(N), \quad (5)$$

where $\langle g_{12}(\tau_3) \rangle_{\text{M3}}$ corresponds to an averaged, elementary step length between two successive renewal events (abbreviated as M3), and is characterized by the intramolecular transport mechanisms (i. e. the diffusion along the chain and the polymer dynamics). The center-of-mass motion of the PEO chains with length N is characterized by the diffusion coefficient D_{PEO} . As shown in earlier work²⁰, g_{12} can be described by a Rouse-like

expression

$$g_{12}(t) = \frac{2\langle \mathbf{R}_e^2 \rangle}{\pi^2} \sum_{p=1}^{\infty} \frac{[1 - \exp(-\frac{tp^2}{\tau_{12}})]}{p^2}, \quad (6)$$

where $1/\tau_{12} = 1/\tau_1 + 1/\tau_2$ is a combined relaxation rate due to both mechanisms. As argued in Section V, lithium ions coordinated to two PEO chains experience no effective transport due to the diffusion along the chain (see also supporting information of ref. 17). However, with respect to Equation 6, this effect can be easily captured. For a sufficiently fast exchange between coordinations to one and to two PEO chains, the average intramolecular lithium MSD \bar{g}_{12} is simply determined by the structural quantities r_1 and r_2 (Table I):

$$\bar{g}_{12}(t) = r_1 g_{12}(t) + r_2 g_2(t) \quad (7)$$

That is, for the fraction r_1 of cations bound to one PEO chain, Equation 6 remains valid, whereas for ions bound to two chains with $\tau_{1,2\text{PEO}} \rightarrow \infty$, only τ_2 is important. For exponentially distributed residence times at the distinct PEO chains (which is fulfilled to a good approximation in our simulations except for shortest residence times lower than 300 ps, which account only for a few percent), one can write down an analytical expression for the average MSD at a given chain:

$$\begin{aligned} \langle g_{12}(\tau_3) \rangle_{\text{M3}} &= \frac{1}{\tau_3} \int_0^{\infty} dt \exp\left(-\frac{t}{\tau_3}\right) g_{12}(t) \\ &= \frac{2\langle \mathbf{R}_e^2 \rangle}{\pi^2} \sum_{p=1}^{\infty} \frac{1}{p^2} \left[1 - \frac{1}{p^2 \frac{\tau_3}{\tau_{12}} + 1} \right] \end{aligned} \quad (8)$$

Solving this expression numerically, values for D_{Li} were obtained for $N = 54$ ($D_{\text{Li}}^{\text{sim}}$) and $N \rightarrow \infty$ (D_{Li}^{∞}), which are summarized in Table IV (here, a correction similar to Equation 7 has been applied). For the calculation of $D_{\text{Li}}^{\text{sim}}$, D_{PEO} was simply extracted from the simulation. When comparing $D_{\text{Li}}^{\text{sim}}$ with the lithium diffusion coefficients directly extracted from Figure 4, we find reasonable agreement between both values (although the diffusion coefficients from the MSDs are about 5 – 20 % higher, which is due to the fact that the lithium motion has not yet become fully diffusive and the statistical uncertainties are relatively large in the long-time regime). However, when using the transport model to calculate the lithium MSDs as in our previous work¹⁷ (which was done by simulating a random-walk motion whose step length was given by Equation 6, and in which random reorientations at given time steps sampled from a Poisson process modeled the renewal events), we find quantitative agreement within the error bars for all systems, showing that the predictions of our model are consistent with the numerical data.

In the following, we will compare our results with the experimental data ($D_{\text{Li}}^{\text{exp}}$) at $T = 323$ K taken from ref. 12. Despite the temperature gap between simulation and experiment, we observe identical trends: For a

system	$D_{\text{Li}}^{\text{sim}} [\text{\AA}^2\text{ns}^{-1}]$	$D_{\text{Li}}^{\infty} [\text{\AA}^2\text{ns}^{-1}]$	$D_{\text{Li}}^{\text{exp}} [\text{\AA}^2\text{ns}^{-1}]$ (ref. 12)
P ₂₀ S	2.945 (2.947)	1.947 (1.949)	0.052 (P ₂₀ S · 1.0 IL)
P ₂₀ S · x IL			
P ₂₀ S · 0.66 IL	3.542 (3.545)	2.309 (2.313)	0.118 (P ₂₀ S · 2.0 IL)
P ₂₀ S · 3.24 IL	4.257 (4.292)	2.392 (2.434)	0.126 (P ₂₀ S · 4.0 IL)
P _{20-αx} S · x IL			
P ₁₆ S · 0.556 IL	2.573 (2.581)	1.511 (1.520)	0.051 (P ₁₀ S · 1.0 IL)
P ₁₂ S · 1.111 IL	2.716 (2.765)	1.311 (1.366)	0.063 (P ₁₀ S · 2.0 IL)
P ₈ S · 1.667 IL	2.812 (3.092)	1.166 (1.487)	0.046 (P ₅ S · 1.0 IL)

Table IV: Lithium diffusion coefficient D_{Li} calculated by the lithium transport model (in particular Equations 5 and 8) for $N = 54$ ($D_{\text{Li}}^{\text{sim}}$) and $N \rightarrow \infty$ (D_{Li}^{∞}). The values in parentheses for $D_{\text{Li}}^{\text{sim}}$ and D_{Li}^{∞} are corrected values, for which the lithium migration through IL-rich regions has been taken into account. Experimental values¹² for similar compositions at $T = 323$ K are also shown.

similar dilution series, in which the IL is *added* to P₂₀S, $D_{\text{Li}}^{\text{exp}}$ also increases significantly with increasing IL content. In contrast to this, $D_{\text{Li}}^{\text{exp}}$ rather decreases when the PEO chains are *substituted* by IL, and, consequently, the EO : Li ratio decreases.

As already discussed in context with the segmental PEO motion (Section V A), these observations can be understood as follows: In case of P₂₀S · x IL, the IL acts as a plasticizer, and the enhanced polymer dynamics leads to a faster lithium ion dynamics. On the other hand, when the EO : Li ratio simultaneously decreases as for P_{20- αx} S · x IL, the remaining PEO chains become more and more rigid, which approximately cancels the plasticizing effect of the IL.

Thus, two opposing trends related to the segmental mobility can be found in ternary polymer electrolyte-ionic liquid mixtures: the slowdown of the polymer motion with decreasing EO : Li ratio (also encountered in the binary systems) and the plasticizing due to the IL, leading to an enhancement of the polymer dynamics (i. e. both the segmental and the center-of-mass motion). Naturally, for the technologically relevant long-chain limit, the enhancement of the center-of-mass motion of the PEO chains is irrelevant. For these reasons, one should keep in mind that especially the polymer segments remain mobile enough when designing new electrolyte materials.

It should be pointed out that the D_{Li} -values in Table IV do not contain the contribution from those lithium ions which are coordinated by IL molecules only and thus move faster. In particular for the electrolytes P₁₂S · 1.111 IL and P₈S · 1.667 IL, for which this additional, fourth mechanism becomes relevant (Table II), this would lead to noticeably higher D_{Li} -values in Table IV. Here, a correction to D_{Li} can easily be estimated: At a given time, the fraction of lithium ions coordinated by TFSI only is given by p_{IL} (Table II). Since we found that dynamics of these ions is similar to that in PYR₁₃TFSI · 0.262 LiTFSI, one can use the respective lithium diffusion coefficient ($D_{\text{Li,IL}} = 14.014 \text{\AA}^2\text{ns}^{-1}$) to estimate their contribution to the overall diffusion coefficient, whereas the relative contribution of the remaining

lithium ions is still described by Equation 5:

$$D_{\text{Li}}^{\text{corr}}(N) = (1 - p_{\text{IL}}) D_{\text{Li}}(N) + p_{\text{IL}} D_{\text{Li,IL}} \quad (9)$$

The respective corrected values for $D_{\text{Li}}^{\text{sim}}$ and D_{Li}^{∞} are given in parentheses in Table IV. As already expected from the values of p_{IL} , significant contributions arise only for P₁₂S · 1.111 IL and P₈S · 1.667 IL ($p_{\text{IL}} = 0.4$ % and 2.5 %, respectively), whereas D_{Li} for all other electrolytes remains basically unaltered.

Thus, for most electrolytes, the value of D_{Li} is determined by essentially three contributions (Equation 5): the intrachain distance $\langle g_{12}(\tau_3) \rangle_{\text{M3}}$ the ion covers while connected to the same chain, the center-of-mass motion of the PEO molecules characterized by D_{PEO} and the renewal events measured by τ_3 , which facilitate the diffusive motion of the ions in the long-time limit for $N \rightarrow \infty$. Moreover, these trends may also oppose each other as in case of P₂₀S · x IL. For these reasons, it is desirable to quantify in how far the modified intrachain transport and the altered renewal rates contribute to the overall change of D_{Li} relative to the pure polymer electrolyte P₂₀S.

Table V shows the percentage by which the intramolecular contributions ($\langle g_{12}(\tau_3) \rangle_{\text{M3}}$), the center-of-mass motion of the PEO chains (D_{PEO}) and the renewal rates (τ_3^{-1}) as well as the overall D_{Li} -values change relative to the pure polymer electrolyte P₂₀S for $N = 54$ and $N \rightarrow \infty$.

For P₂₀S · x IL one clearly observes that the intramolecular contribution increases with the IL concentration, mainly as a result of the increased segmental mobility. For finite PEO chains, the enhanced D_{PEO} -value additionally increases the lithium motion. In contrast to this, the contribution of the renewal processes decreases for these electrolytes. However, the plasticizing effect overcompensates this decrease, and D_{Li} increases for both $N = 54$ and $N \rightarrow \infty$.

Remarkably, the relative intramolecular contribution also increases for P_{20- αx} S · x IL, although the enhancement is weaker than for P₂₀S · x IL. At first glance, this may contradict the findings presented in Section V A, where it was observed that both the diffusion along the PEO chain and the segmental motion become slower

(a) $N = 54$				
system	$\langle g_{12}(\tau_3) \rangle_{M3}$	τ_3^{-1}	D_{PEO}	D_{Li}
P ₂₀ S	± 0	± 0	± 0	± 0
P ₂₀ S · x IL				
P ₂₀ S · 0.66 IL	+22	-7	+30	+20
P ₂₀ S · 3.24 IL	+54	-29	+92	+45
P _{20-αx} S · x IL				
P ₁₆ S · 0.556 IL	+9	-32	+4	-13
P ₁₂ S · 1.111 IL	+6	-40	+30	-8
P ₈ S · 1.667 IL	+5	-48	+50	-5

(b) $N \rightarrow \infty$				
system	$\langle g_{12}(\tau_3) \rangle_{M3}$	τ_3^{-1}	D_{PEO}	D_{Li}
P ₂₀ S	± 0	± 0	-	± 0
P ₂₀ S · x IL				
P ₂₀ S · 0.66 IL	+28	-7	-	+19
P ₂₀ S · 3.24 IL	+73	-29	-	+23
P _{20-αx} S · x IL				
P ₁₆ S · 0.556 IL	+14	-32	-	-22
P ₁₂ S · 1.111 IL	+12	-40	-	-33
P ₈ S · 1.667 IL	+15	-48	-	-40

Table V: Percental changes of the intramolecular contribution $\langle g_{12}(\tau_3) \rangle_{M3}$, the renewal rates τ_3^{-1} , the center-of-mass motion D_{PEO} and the resulting D_{Li} -value relative to P₂₀S for (a) $N = 54$ and (b) $N \rightarrow \infty$.

when IL is added to the system. However, this mismatch can easily be resolved by the following considerations: First, the fraction of lithium ions coordinated to one PEO chain only increases when going from P₂₀S to P₈S · 1.667 IL (Table I). Since lithium ions coordinated to two polymer chains experience no effective transport via this mechanism (supporting information in ref. 17), the diffusion along the PEO backbone becomes more efficient in this way. The second, more important effect leading to the observations from Table V is the fact that $\langle g_{12}(\tau_3) \rangle_{M3}$ is evaluated for different τ_3 (Equation 8). Thus, with increasing τ_3 also the distance $\langle g_{12}(\tau_3) \rangle_{M3}$ increases, although this dependence is weaker than linear, and the overall D_{Li} diminishes in this case. Consistently, calculating the individual values for $\langle g_{12}(\tau_3) \rangle_{M3}$ with a constant value of $\tau_3 = 17.1$ ns as observed for P₂₀S (Table II), the intramolecular contribution indeed decreases for P_{20- α x}S · x IL. The only contribution which displays a clear increase is D_{PEO} . Thus, for $N = 54$, D_{Li} diminishes only slightly, whereas a significant decrease can be found in case of $N \rightarrow \infty$.

So far, we focused only on the high-temperature limit which we can address in our simulations. Interestingly, the relative increase of D_{Li}^{exp} upon the addition of IL becomes much more pronounced in the low-temperature regime¹². Although simulations at low temperature would be too costly, we are nevertheless able to make some statements about this regime. For example, in case of the addition of IL, it was reported that the glass-

transition temperature T_g significantly decreases (up to 35 K) with increasing IL concentration¹², which is a first indication that also at ambient temperatures the enhanced polymer dynamics contributes to a larger D_{Li} . In contrast to this, the experimentally observed decrease of T_g is significantly weaker for lower EO : Li ratios¹² (which resembles the case of IL substitution). Simultaneously, D_{Li}^{exp} approximately remains constant at 323 K. A detailed analysis of the low-temperature regime is already underway.

VII. CONCLUSION

In this work, we presented an exhaustive MD simulation study on ternary polymer electrolytes consisting of PEO/LiTFSI and the ionic liquid PYR₁₃TFSI. In total, we investigated two different concentration series, namely (a) the *addition* of the ionic liquid to PEO₂₀LiTFSI, and (b) the *substitution* of the PEO chains in PEO₂₀LiTFSI by the ionic liquid, subject to the constraint of a constant lithium volume concentration. The latter electrolytes not only reflected an interpolation between PEO₂₀LiTFSI and PYR₁₃TFSI · 0.262 LiTFSI, but also served as model systems for electrolytes with lower EO : Li ratios. In addition to the simulations, we also utilized a lithium ion transport model²⁰ to express the effect of the ionic liquid on the lithium diffusion via a few microscopic parameters. Based on the combined insights from the simulations and the transport model, we were able to formulate general statements in how far the lithium ion transport mechanism changes when the composition of the electrolyte is varied.

In case of sufficiently high EO : Li ratios (in particular 20 : 1), we find that the lithium transport almost exclusively takes place at the PEO chains, and that the transport mechanism therefore is qualitatively the same as in binary PEO₂₀LiTFSI. For lower ratios, however, more and more lithium ions coordinate to a specific PEO chain, with the result that a progressive coordination by TFSI anions (both partially and totally) becomes visible. Accordingly, a completely new, fourth transport mechanism, in which the lithium ions are decoupled from the PEO chains, emerges due to the lack of free ether oxygens capable to bind the lithium ions. This mechanism may significantly contribute to the macroscopic lithium diffusion or even dominate it. From a theoretical perspective, we incorporated this mechanism into our transport model. For all electrolytes, we find reasonable agreement of the model predictions with the experimentally observed diffusion coefficients¹².

Apart from these qualitative differences, the lithium transport is also altered on a quantitative level. For instance, the renewal rate τ_3^{-1} , characterizing the transfer between distinct PEO chains, decreases with increasing ionic-liquid concentration and with decreasing fraction of free ether oxygens. Consequently, τ_3 is especially large for diluted electrolytes with crowded PEO chains (i.e.

system	L_{box} [Å]
PEO	40.11
P ₂₀ S	35.96
P ₂₀ S · x IL	
P ₂₀ S · 0.66 IL	38.27
P ₂₀ S · 3.24 IL	45.29
P _{20-αx} S · x IL	
P ₁₆ S · 0.556 IL	35.93
P ₁₂ S · 1.111 IL	35.96
P ₈ S · 1.667 IL	36.00
IL · 0.262 S	36.33

Table VI: Length of the simulation boxes for the different electrolytes.

the PEO_{20- α x}LiTFSI · x PYR₁₃TFSI systems).

Concerning the polymer dynamics, it turned out that the increase of the lithium diffusivity in PEO₂₀LiTFSI · x PYR₁₃TFSI can be attributed to the enhanced segmental mobility of the PEO chains, and that the ionic liquid thus serves as a plasticizer. As a result of the faster PEO motion, also the lithium ions coordinating to the PEO chains become faster. Interestingly, the plasticization is also visible in the scaling of the Rouse-mode relaxation times, which exhibit a slightly Zimm-like scaling characteristic for semidilute polymer solutions. An opposing effect on the PEO dynamics, however, is the coordination to the lithium ions, which becomes especially pronounced for low EO : Li ratios. Accordingly, the average PEO dynamics in PEO_{20- α x}LiTFSI · x PYR₁₃TFSI is slowed down by the progressive coordination of lithium ions, and the plasticizing effect of the ionic liquid becomes visible only for larger, entirely uncoordinated polymer segments. In summary, one therefore faces the situation that the segmental mobility of the PEO chains plays a decisive role in ternary polymer electrolytes: Whereas the lithium ions slow down the PEO chains, the ionic liquid accelerates the polymer motion. Thus, for the design of new battery materials, one should attempt to render the latter effect the dominating one.

Acknowledgments

The authors would like to thank Oleg Borodin, Nicolaas A. Stolwijk, Stefano Passerini and Mario Joost for helpful discussions and for providing the experimental data. Financial support from the NRW Graduate School of Chemistry is also greatly appreciated.

Appendix A: Part A: Further Analyses

1. Simulation Box Size

The sizes of the individual simulation boxes are summarized in Table VI. One clearly observes that while for the P₂₀S · x IL systems the volume of the simulation box increases, L_{box} for the P_{20- α x}S · x IL electrolytes is nearly identical for each system, meaning that the lithium volume concentration (27 lithium ions in each box) remains constant.

2. Radial Distribution Functions

Figure 10 shows the radial distribution functions $g(r)$ for the atom pairs Li⁺ – O_{PEO} and Li⁺ – O_{TFSI}. Both coordination types exhibit a sharp peak around 2 Å corresponding to the first coordination shell. For Li⁺ – O_{PEO}, the first coordination sphere directly crosses over into a second small peak around 3.3 Å. At larger distances no significant structural arrangement can be found. For the coordination of Li⁺ – O_{TFSI}, peaks become noticeable also at larger distances around 6 Å and 8 Å, thus demonstrating that long-ranged correlations are present as also observed for a PEO₂₀LiI electrolyte⁴⁵. The same observation can be made for the PEO-free electrolyte PYR₁₃TFSI · 0.262 LiTFSI, as also reported in previous MD studies³⁵. The pair correlation function of the PYR₁₃ cations and TFSI anions (i.e. N_{PYR₁₃} – O_{TFSI}) exhibits only a weak first coordination peak between 3.6 and 5.0 Å.

When successively adding the IL, one observes that the peak positions of both Li⁺ – O_{PEO} and Li⁺ – O_{TFSI} remain the same for all electrolytes. For P₂₀S · x IL, the EO coordination numbers extracted from the integral over the first shell increase slightly, partly as a result of the lower fraction of lithium ions coordinating to two PEO chains (Table I in the main article), for which the EO coordination number is lower due to steric effects. In P_{20- α x}S · x IL, the absolute EO coordination number (as determined from the integral over $g(r)$) decreases with increasing IL content. This trend can be explained by the decreasing number of possible coordination sites, since the PEO concentration reduces. Naturally, the coordination number of the TFSI oxygens increases with increasing IL content in both types of electrolytes.

3. Lithium Coordination Shell

Figure 11 shows the probability distribution functions $p(n)$ to find a lithium ion with n EOs or TFSI oxygens in its first coordination shell. One observes that for PEO₂₀LiTFSI · x PYR₁₃TFSI, the coordination numbers are very similar in all systems and only change slightly with the IL concentration. In contrast to this, for P_{20- α x}S · x IL, a coordination number of $n = 2$ EOs

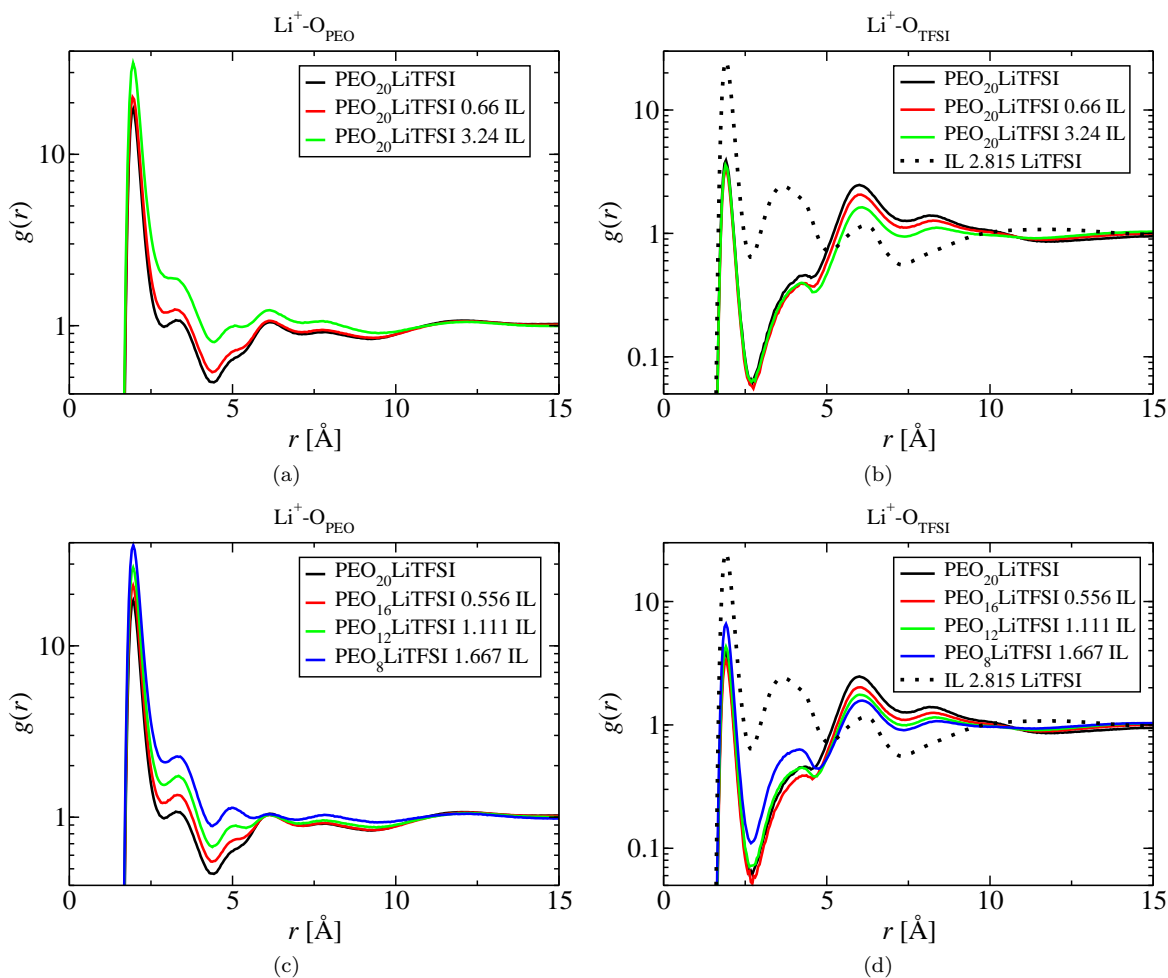


Figure 10: Upper: radial distribution functions in $\text{P}_{20}\text{S} \cdot x \text{ IL}$ for the atom pairs (a) $\text{Li}^+ - \text{O}_{\text{PEO}}$ and (b) $\text{Li}^+ - \text{O}_{\text{TFSI}}$. Lower: radial distribution functions in $\text{P}_{20-\alpha x}\text{S} \cdot x \text{ IL}$ for the atom pairs (c) $\text{Li}^+ - \text{O}_{\text{PEO}}$ and (d) $\text{Li}^+ - \text{O}_{\text{TFSI}}$.

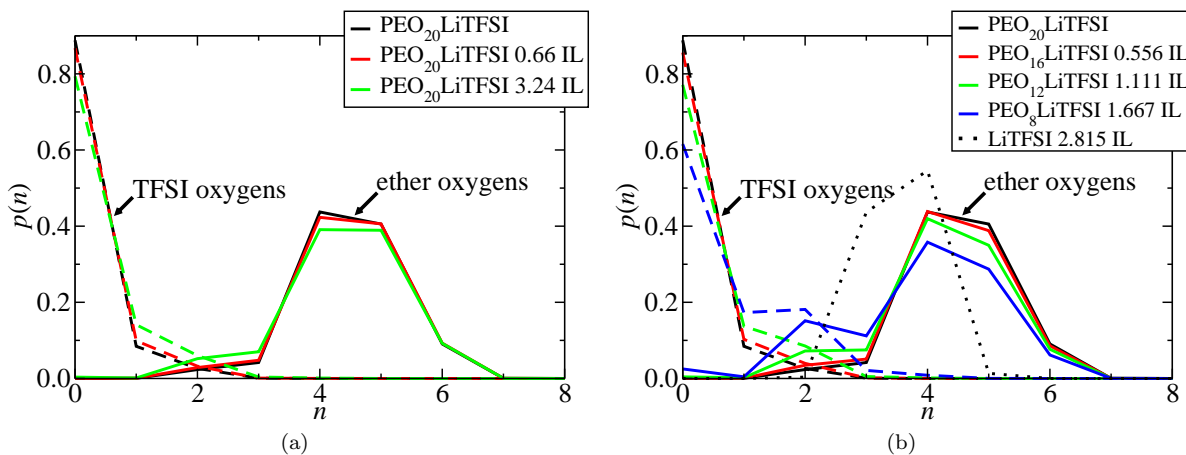


Figure 11: Probability $p(n)$ to find a certain coordination number n of EOs (irrespective if the ion is tied to one or two PEO chains) or TFSI oxygens in (a) $\text{P}_{20}\text{S} \cdot x \text{ IL}$ and (b) $\text{P}_{20-\alpha x}\text{S} \cdot x \text{ IL}$.

becomes noticeable, and simultaneously the probability for one or two coordinating anions increases.

Appendix B: Part B: Force Field Validation

In order to validate the results from the AMBER simulations, comparative simulations with Lucretius⁴⁶ (the original code for which the force field used in this study has been developed) have been performed. We focus on the pure polymer electrolyte PEO₂₀LiTFSI. For the Lucretius simulation, the same techniques and parameters as in the original study⁴⁷ have been used. Both MD codes yielded the same density when simulating an NpT ensemble, thus giving a first indication that the AMBER results are reasonable. In the following, NVT simulations of the respective codes will be compared (the results are the same for NpT simulations). Since the Lucretius version used in this comparison (i. e. the same as in ref. 47) does not allow parallel calculations, the total simulation length was restricted to 50 ns as compared to the 200 ns of the AMBER simulations (note that in the meantime a newer, parallelized Lucretius version is also available).

1. Dihedral Distributions

Figure 12 shows the probability distribution function $p(\phi)$ of the dihedral angles ϕ describing the rotation around the carbon-carbon (O-C-C-O) and the carbon-oxygen (C-O-C-C) bonds of the PEO backbone. For the O-C-C-O-dihedral, one observes perfect agreement between the two codes, whereas for the conformations of the C-O-C-C-dihedral slight differences can be observed. These deviations can be rationalized by the fact that the bond length constraining (SHAKE²⁹) for non-hydrogen bonds is not possible in parallel AMBER simulations. Since these bonds can be stretched in these simulations, the 1-4 repulsions between the outer carbon atoms of the C-O-C-C-dihedral is mitigated, and the *gauche*-conformation ($\phi \approx 75^\circ$) becomes more populated compared to the *trans*-conformation ($\phi = 180^\circ$). Indeed, the same observation can be made for a Lucretius simulation (length 25 ns) without bond length constraining. However, these slight deviations have no influence on the dynamics of the PEO backbone and the lithium motion (see discussion below).

2. Radial Distribution Functions

Figure 13 shows the radial distribution functions $g(r)$ for the $\text{Li}^+ - \text{O}_{\text{PEO}}$ and the $\text{Li}^+ - \text{O}_{\text{TFSI}}$ interaction. For both coordination types one observes reasonable agreement. Again, the slight deviations for the second coordination peak are related to the fact that the molecules

in AMBER are more flexible due to the unconstrained bonds.

3. Mean Square Displacements

Figure 14 shows the MSDs for the individual molecular species in PEO₂₀LiTFSI. Since the AMBER simulation extends over 200 ns and the MSDs thus have much smaller error bars, only the error bars of the Lucretius curves are shown for clarity. For PEO, an additional distinction was made between the segmental dynamics (EOs) and center-of-mass motion. The agreement for all molecule types is quantitative. Deviations for larger time scale of several ten nanoseconds are within the error bars of the shorter Lucretius simulation. In total, the agreement between the two MD codes is convincing.

Appendix C: Part C: Benchmark Calculations

Benchmark calculations have been performed for the modified AMBER code. Again, we focus on the electrolyte PEO₂₀LiTFSI (4772 atoms) at $T = 423$ K in the NVT ensemble using various numbers of CPUs (Intel Xeon Nehalem X5550 with 2.67 GHz each, PALMA cluster⁴⁸). The simulations were carried out using various treatments of the polarization, in particular without polarization, iterative solution of the inducible dipoles, as well as the Car-Parrinello scheme described in ref. 30.

The computation time is shown in Figure 15. For convenience, the resulting MD time per day is also shown in Figure 15. For small processor numbers, one observes an ideal linear increase of the computation speed. From about eight CPUs this scaling drops below linear scaling, and finally saturates at a maximum computation speed for 32 CPUs. A more detailed analysis of the computation times of the distinct contributions (i. e. bonded, van-der-Waals or electrostatic interactions) reveals that the saturation as well as the subsequent decrease in Figure 15 arises from the evaluation of the reciprocal part of the electrostatic energies and forces. For this step, all spatial coordinates of the system are involved in the calculation, requiring the excessive communication between the individual CPUs. Consequently, the speed-up gained by the larger number of CPUs cannot compensate for this massive broadcast, so that the real computation time saturates and finally decreases again.

The incorporation of polarization leads to a decrease of the simulation speed. Here, the Car-Parrinello-like treatment of the dipoles³⁰ is significantly faster than the iterative solution of the inducible dipoles. For many CPUs, their relative difference becomes even larger. As discussed above, this effect is related to the enormous broadcast and the exchange of the inducible dipoles between the individual CPUs. This slowdown becomes especially heavy for the iterative scheme, as the dipoles have to be

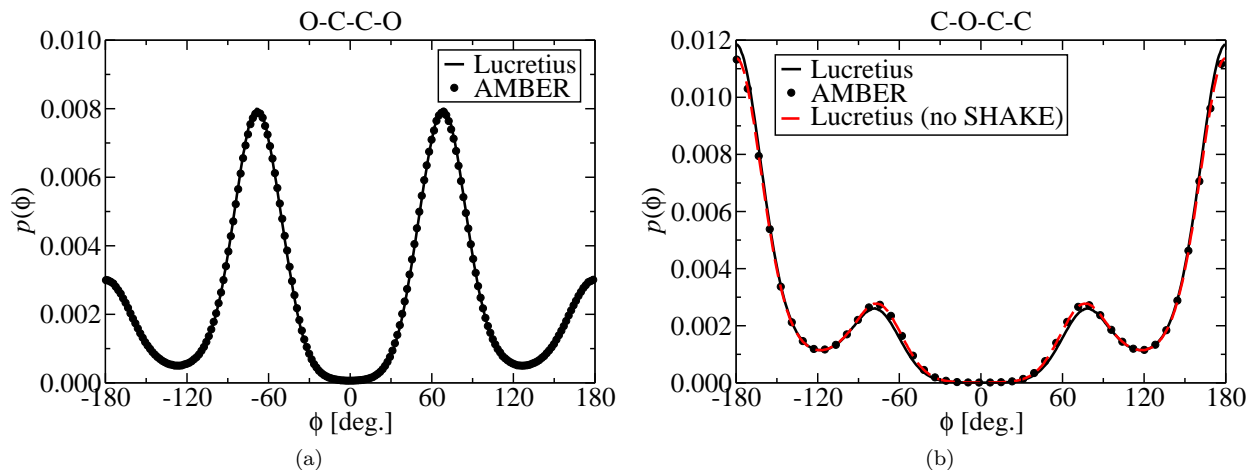


Figure 12: Probability distribution function of two dihedral types of the PEO backbone for $\text{PEO}_{20}\text{LiTFSI}$ at $T = 423$ K. (a) O-C-C-O and (b) C-O-C-C.

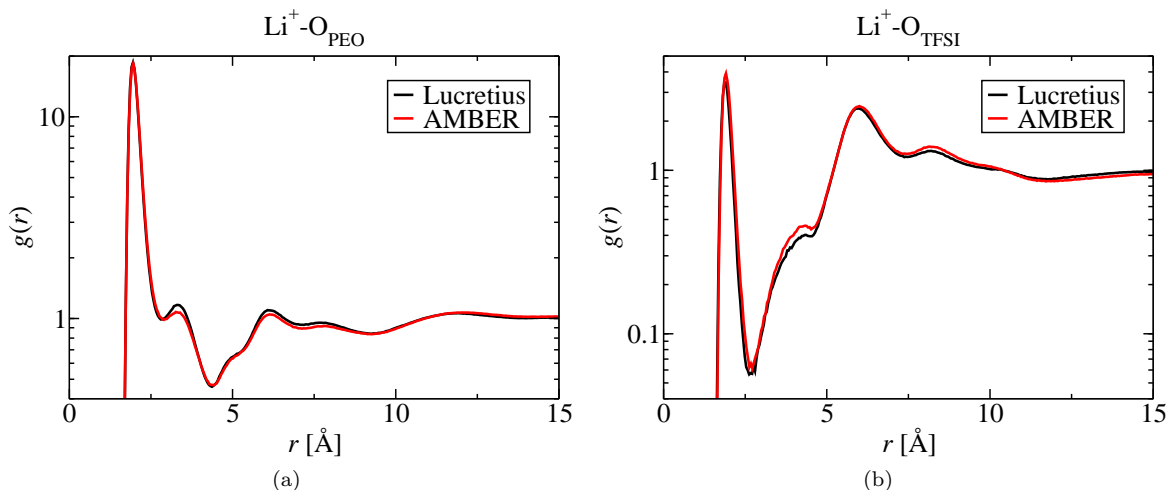


Figure 13: Radial distribution functions $g(r)$ of the (a) $\text{Li}^+-\text{O}_{\text{PEO}}$ and the (b) $\text{Li}^+-\text{O}_{\text{TFSI}}$ interaction.

gathered and redistributed on the nodes in each iteration step.

* Electronic address: d.diddens@uni-muenster.de

¹ D. E. Fenton, J. M. Parker, and P. V. Wright, *Polymer* **14**, 589 (1973).

² M. B. Armand, *Ann. Rev. Mater. Sci.* **16**, 245 (1986).

³ F. M. Gray, *Solid Polymer Electrolytes* (Wiley-VCH, New York, 1991).

⁴ P. G. Bruce and C. A. Vincent, *Journal of the Chemical Society, Faraday Transactions* **89**, 3187 (1993).

⁵ W. Gang, J. Roos, D. Brinkmann, F. Capuano, F. Croce, and B. Scrosati, *Solid State Ionics* **53**, 1102 (1992).

⁶ M. C. Borghini, M. Mastragostino, and A. Zanelli, *Electrochimica Acta* **41**, 2369 (1996).

⁷ L. R. A. K. Bandara, M. A. K. L. Dissanayake, and B. E. Mellander, *Electrochimica Acta* **43**, 1447 (1998).

⁸ Y. T. Kim and E. S. Smotkin, *Solid State Ionics* **149**, 29

(2002).

⁹ J. H. Shin, W. A. Henderson, and S. Passerini, *Electrochemistry Communications* **5**, 1016 (2003).

¹⁰ J. H. Shin, W. A. Henderson, G. B. Appetecchi, E. Alessandrini, and S. Passerini, *Electrochimica Acta* **50**, 3859 (2005).

¹¹ J. H. Shin, W. A. Henderson, S. Scaccia, P. P. Prosini, and S. Passerini, *Journal of Power Sources* **156**, 560 (2006).

¹² M. Joost, M. Kunze, S. Jeong, M. Schönhoff, M. Winter, and S. Passerini, *Electrochim. Acta* **86**, 330 (2012).

¹³ D. Adam, *Nature* **407**, 938 (2000).

¹⁴ D. R. MacFarlane, J. H. Huang, and M. Forsyth, *Nature* **402**, 792 (1999).

¹⁵ D. R. MacFarlane, P. Meakin, J. Sun, N. Amini, and M. Forsyth, *Journal of Physical Chemistry B* **103**, 4164

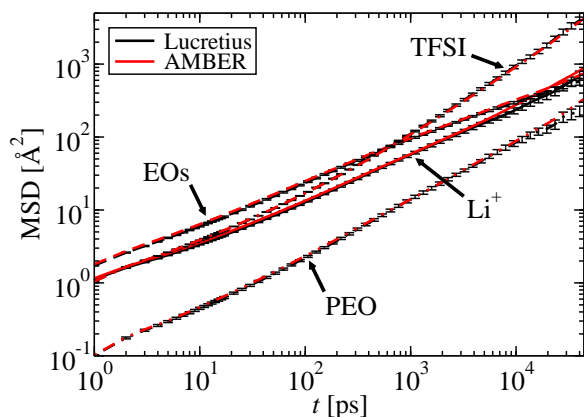


Figure 14: MSDs for the individual molecule types in PEO₂₀LiTFSI simulated with Lucretius and AMBER.

- (1999).
- ¹⁶ Q. Zhou, W. A. Henderson, G. B. Appetecchi, M. Montanino, and S. Passerini, *Journal of Physical Chemistry B* **112**, 13577 (2008).
 - ¹⁷ D. Diddens and A. Heuer, *ACS Macro Letters* **2**, 322 (2013).
 - ¹⁸ I. Nicotera, C. Oliviero, W. Henderson, G. Appetecchi, and S. Passerini, *Journal of Physical Chemistry B* **109**, 22814 (2005).
 - ¹⁹ M. Kunze, E. Paillard, S. Jeong, G. B. Appetecchi, M. Schoenhoff, M. Winter, and S. Passerini, *Journal of Physical Chemistry C* **115**, 19431 (2011).
 - ²⁰ A. Maitra and A. Heuer, *Physical Review Letters* **98**, 227802 (2007).
 - ²¹ P. E. Rouse, *Journal of Chemical Physics* **21**, 1272 (1953).
 - ²² A. Nitzan and M. A. Ratner, *J. Phys. Chem.* **98**, 1765 (1994).
 - ²³ D. A. Case, T. A. Darden, T. E. Cheatham, C. L. Simmerling, J. Wang, R. E. Duke, R. Luo, M. Crowley, R. C. Walker, W. Zhang, et al., *Amber 10* (University of California, San Francisco, 2008), URL <http://amber.scripps.edu/#Amber10>.
 - ²⁴ O. Borodin and G. D. Smith, *Journal of Physical Chemistry B* **110**, 6279 (2006).
 - ²⁵ O. Borodin and G. D. Smith, *Journal of Physical Chemistry B* **110**, 6293 (2006).
 - ²⁶ O. Borodin and G. D. Smith, *Journal of Physical Chemistry B* **110**, 11481 (2006).
 - ²⁷ A. Toukmaji, C. Sagui, J. Board, and T. Darden, *Journal of Chemical Physics* **113**, 10913 (2000).
 - ²⁸ H. J. C. Berendsen, J. P. M. Postma, W. F. van Gunsteren, A. DiNola, and J. R. Haak, *Journal of Chemical Physics* **81**, 3684 (1984).
 - ²⁹ J. P. Ryckaert, G. Ciccotti, and H. J. C. Berendsen, *Journal of Computational Physics* **23**, 327 (1977).
 - ³⁰ D. van Belle, M. Froeyen, G. Lippens, and S. J. Wodak, *Molecular Physics* **77**, 239 (1992).
 - ³¹ B. T. Thole, *Chemical Physics* **59**, 341 (1981).
 - ³² G. Mao, M.-L. Saboungi, D. L. Price, M. B. Armand, and W. S. Howells, *Physical Review Letters* **84**, 5536 (2000).
 - ³³ P. Johansson, J. Tegenfeld, and J. Lindgren, *Polymer* **40**, 4399 (1999).
 - ³⁴ A. G. Baboul, P. C. Redfern, A. Sutjianto, and L. A. Curtiss, *Journal of the American Chemical Society* **121**, 7220 (1999).
 - ³⁵ O. Borodin, G. D. Smith, and W. Henderson, *Journal of Physical Chemistry B* **110**, 16879 (2006).
 - ³⁶ J.-C. Lassegues, J. Grondin, and D. Talaga, *Physical Chemistry Chemical Physics* **8**, 5629 (2006).
 - ³⁷ M. Doi and S. F. Edwards, *The Theory of Polymer Dynamics* (Oxford Science Publications, Clarendon, Oxford, 2003).
 - ³⁸ P. H. Verdier, *Journal of Chemical Physics* **45**, 2118 (1966).
 - ³⁹ D. Diddens, A. Heuer, and O. Borodin, *Macromolecules* **43**, 2028 (2010).
 - ⁴⁰ B. H. Zimm, *Journal of Chemical Physics* **24**, 269 (1956).
 - ⁴¹ P. Ahlrichs, R. Everaers, and B. Dünweg, *Physical Review E* **64** (2001).
 - ⁴² P. Ahlrichs and B. Dünweg, *Journal of Chemical Physics* **111**, 8225 (1999).
 - ⁴³ M. Appel and G. Fleischer, *Macromolecules* **26**, 5520 (1993).
 - ⁴⁴ J. Shi and C. A. Vincent, *Solid State Ionics* **60**, 11 (1993).
 - ⁴⁵ A. Maitra and A. Heuer, *Journal of Physical Chemistry B* **112**, 9641 (2008).
 - ⁴⁶ G. D. Smith, C. Ayyagari, D. Bedrov, and O. Borodin, *Lucretius-v.3.0* (2004), <http://www.eng.utah.edu/~gdsmith/lucretius.html>.
 - ⁴⁷ O. Borodin and G. D. Smith, *Macromolecules* **39**, 1620 (2006).
 - ⁴⁸ W. W.-U. M. Zentrum für Informationsverarbeitung, *Palma: Paralleles linux-system für münsteraner anwender* (2010), <http://www.uni-muenster.de/ZIV/Technik/Server/HPC-PALMA.html>.

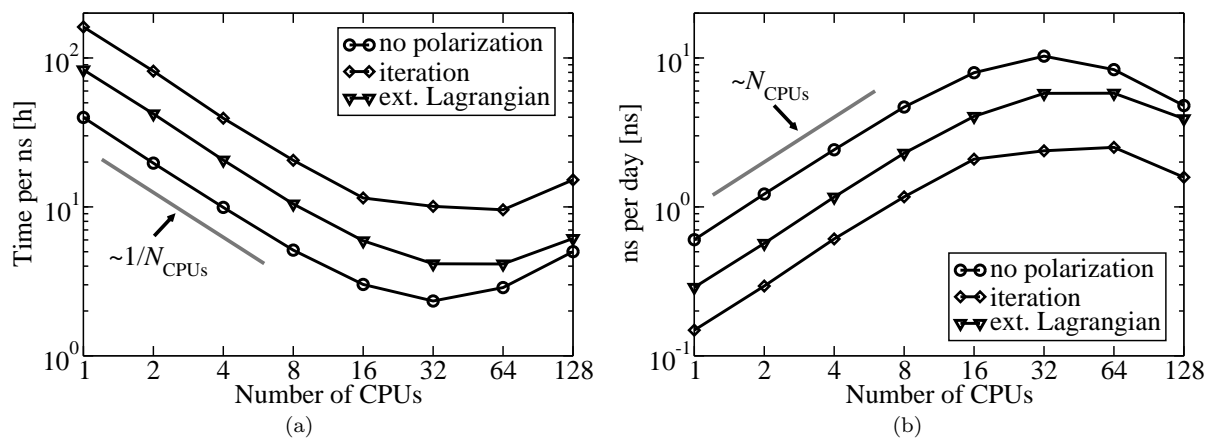


Figure 15: Computation time for PEO₂₀LiTFSI (4772 atoms) in dependence of the number of CPUs for various polarization treatments. For convenience, the accessible MD time per day is also shown.